solids

MDPI

Review

MXene-Based Composites for Energy Harvesting and Energy Storage Devices

Jorge Alexandre Alencar Fotius [1,2] and Helinando Pequeno de Oliveira [2,*]

[1] Instituto Federal de Educação, Ciência e Tecnologia do Sertão Pernambucano, Petrolina 56316-686, PE, Brazil; jorge.fotius@ifsertao-pe.edu.br
[2] Instituto de Pesquisa em Ciência dos Materiais, Universidade Federal do Vale do São Francisco, Juazeiro 48902-300, BA, Brazil
* Correspondence: helinando.oliveira@univasf.edu.br

Abstract

MXenes, a class of two-dimensional transition metal carbides and nitrides, emerged as a promising material for next-generation energy storage and corresponding applications due to their unique combination of high electrical conductivity, tunable surface chemistry, and lamellar structure. This review highlights recent advances in MXene-based composites, focusing on their integration into electrode architectures for the development of supercapacitors, batteries, and multifunctional devices, including triboelectric nanogenerators. It serves as a comprehensive overview of the multifunctional capabilities of MXene-based composites and their role in advancing efficient, flexible, and sustainable energy and sensing technologies, outlining how MXene-based systems are poised to redefine multifunctional energy platforms. Electrochemical performance optimization strategies are discussed by considering surface functionalization, interlayer engineering, scalable synthesis techniques, and integration with advanced electrolytes, with particular attention paid to the development of hybrid supercapacitors, triboelectric nanogenerators (TENGs), and wearable sensors. These applications are favored due to improved charge storage capability, mechanical properties, and the multifunctionality of MXenes. Despite these aspects, challenges related to long-term stability, sustainable large-scale production, and environmental degradation must still be addressed. Emerging approaches such as three-dimensional self-assembly and artificial intelligence-assisted design are identified as key challenges for overcoming these issues.

Keywords: MXene; supercapacitor electrodes; composites; energy storage; energy harvesting

check for updates

Academic Editor: Xiaolei Sun

Received: 17 June 2025
Revised: 9 July 2025
Accepted: 21 July 2025
Published: 1 August 2025

Citation: Fotius, J.A.A.; Oliveira, H.P.d. MXene-Based Composites for Energy Harvesting and Energy Storage Devices. *Solids* **2025**, *6*, 41. https://doi.org/10.3390/solids6030041

Copyright: © 2025 by the authors. Licensee MDPI, Basel, Switzerland. This article is an open access article distributed under the terms and conditions of the Creative Commons Attribution (CC BY) license (https://creativecommons.org/licenses/by/4.0/).

1. Introduction

Novel structures with tailored properties for energy storage, sensing, and multifunctional devices [1–5] are critical for electronics and advanced engineering-based technologies. In particular, incorporating nanostructures into electrodes for the production of supercapacitors and batteries results from a growing demand for high-efficiency and long-life devices [6,7], which depend on developing materials with high electrical conductivity, large surface areas, and chemical stability. The surface functionalization of nanostructures is widely adopted to enhance electrochemical performance and electrolyte interaction [8–11]. Simultaneously, sensor miniaturization and the development of multifunctional nanostructures have enabled responsive and selective detection platforms for biomedical diagnostics, environmental monitoring, and industrial safety [12–14]. In

parallel, hybrid systems integrating multiple functionalities, such as energy harvesting, storage, and sensing, have gained attention by producing single platforms for self-powered and low-energy-consumption devices, critical for wearable electronics and the Internet of Things (IoT) [15–18]. MXenes have drawn substantial attention among emerging candidates due to their layered structure, high electrical conductivity, and surface versatility [19,20].

Firstly synthesized in 2011 at Drexel University [21], MXenes are two-dimensional (2D) materials derived from MAX phases—layered ceramics composed of transition metals (M), group 13/14 elements (A), and carbon and/or nitrogen (X). The formula $M_{n+1}AX_n$ encompasses a large family of compounds that combine the hardness and thermal stability of ceramics with the conductivity of metals [22,23]. By selectively removing the A element using acidic or molten salt-based methods, MAX phases are transformed into MXenes with highly ordered 2D lamellar structures. Composed of transition metal layers terminated with surface functional groups such as -OH, -F, and -O, these structures offer tunable chemical properties with high electrical conductivity [24]. This unique combination of properties makes MXenes highly attractive for various applications. Their structural characteristics and most common applications are schematically illustrated in Figure 1, which provides an integrated overview of the synthesis pathways, surface functionalization, structural engineering strategies, and broad application scope of MXene-based composites. This diagram highlights the transition from the MAX phase to functional MXenes, the role of intercalants and polymer/CNT hybridization in preventing restacking, and the resulting improvements in electrochemical, sensing, and triboelectric performance.

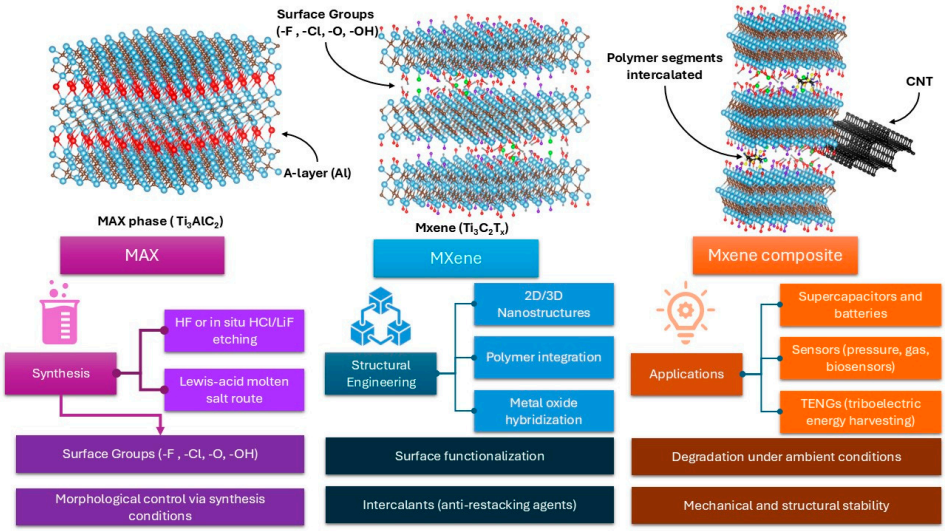


Figure 1. Overview of MXene composite development from MAX phase etching to functionalization with -F, -Cl, -O, and -OH groups. Structural strategies like polymer intercalation and CNT addition enhance ion accessibility and stability, enabling applications in supercapacitors, batteries, sensors, and TENGs.

Their characteristic open-layered structure enables ionic transport, high specific capacitance, and excellent cycling stability [25]. Integration with nanomaterials such as carbon nanotubes (CNTs), graphene, and metal oxides enhances the energy and power densities of MXene while avoiding sheet restacking, which would otherwise degrade its performance. Besides energy storage devices, MXenes have also been explored for sensing and self-powered hybrid devices due to their high surface reactivity, which enables the sensitive detection of gases, biomolecules, and environmental stimuli [26–30]. Their application in triboelectric nanogenerators (TENGs) allows the production of self-powered, wearable devices for harvesting mechanical energy [26,27].

MXene–polymer composites have been incorporated into lightweight, flexible, and electrochemically stable materials in wearable sensors and flexible electronics [31–33]. The reinforcement of these properties is observed using a combination of MXenes, metal oxides, and ceramics, with the resulting materials offering enhanced mechanical strength, thermal stability, and redox ability, enabling high-temperature energy devices and hybrid supercapacitors [34–37]. Similarly, if combined with carbon nanomaterials, MXene derivatives are structured in stable electrodes with higher electrical conductivity and ion-accessible surface areas [38,39]. While these advantages of a multi-component mixture exist, issues such as environmental degradation, sheet restacking, and synthesis scalability remain to be addressed [40]. Recent developments in low-cost green synthesis and advanced functionalization techniques indicate that mass production is becoming more feasible.

Despite their attractive electrochemical properties, MXenes are prone to environmental degradation and structural restacking, affecting their performance. For example, $Ti_3C_2T_x$ films stored in ambient air exhibited a drastic drop in electrical conductivity, falling from approximately 2.49×10^4 $S \cdot m^{-1}$ to less than 7% of the initial value after 27 days, and below 2% after 64 days, due to surface oxidation and the formation of TiO_2 [41]. Similar degradation was observed in aqueous dispersions, with conductivity decreasing by more than 60% within one week of ambient storage [42].

In addition to electrical degradation, MXene oxidation significantly affects structural integrity and mechanical properties, which are critical for energy storage and harvesting applications. Exposure to ambient conditions promotes the formation of TiO_2 nanoparticles, interlayer collapse, and progressive surface disorder, leading to reduced specific surface area and impaired ion transport. These structural changes undermine the electrochemical and mechanical stability of MXene-based electrodes, particularly in flexible devices. Recent studies have demonstrated that water, rather than oxygen, is the dominant factor in MXene degradation, and the surface chemistry of $Ti_3C_2T_x$ strongly influences its oxidation rate in aqueous dispersions. A study demonstrated that MXenes, terminated predominantly with fluorine groups (-F), degrade more rapidly than those with higher contents of oxygen-based terminations (-O and -OH) due to differences in hydrolytic stability and reactivity toward dissolved oxygen [43]. For instance, $Ti_3C_2T_x$ exhibited a degradation time constant of ~5 days in water saturated with O_2, whereas in water under an Ar atmosphere this constant increased to ~41 days. On the other hand, if dispersed in oxygenated isopropanol, the stability exceeded 2000 days, indicating that hydrolysis mechanisms are central to structural breakdown [44]. To mitigate such degradation, both synthesis and storage strategies have been developed. Freezing aqueous dispersions of $Ti_3C_2T_x$ MXene proved a simple and effective method to inhibit oxidation. Samples stored at low temperatures retained their morphology, electrical conductivity, and energy storage performance for up to 650 days, while those stored at room temperature began forming TiO_2 nanoparticles after only 2 days [45]. An effective strategy to extend MXene shelf life involves using sodium dodecyl sulfate (SDS) as an anionic surfactant. It adsorbs onto defect sites via sulfate terminals and forms a steric barrier with its alkyl chains. This protection enabled $Ti_3C_2T_x$ dispersions to remain stable for over 213 days in ambient conditions without compromising electrochemical performance [46]. These findings emphasize the importance of integrating chemical design and physical protection strategies to preserve the structural, electrical, and mechanical functionality of MXene-based materials in real-world applications.

Furthermore, lamellar restacking in MXenes significantly reduces the accessible surface area and limits ion transport pathways. For example, the specific surface area (SSA) of pure $Ti_3C_2T_x$ was reported to be only 8.79 $m^2 \cdot g^{-1}$. In contrast, its incorporation with reduced graphene oxide (rGO) increased this value to 32.4 $m^2 \cdot g^{-1}$ and 59.5 $m^2 \cdot g^{-1}$ when combined with Fe-based nanoparticles due to improved dispersion and the inhibition of

sheet collapse [47]. A similar trend was observed in V_2CT_x-based systems, where the SSA increased from 4.48 $m^2 \cdot g^{-1}$ for pristine V_2CT_x to 8.74 $m^2 \cdot g^{-1}$ in Bi/V_2CT_x composites, accompanied by enhanced mesoporosity [48]. Most notably, nitrogen-doped $Ti_3C_2T_x$ synthesized through NH_4Cl-assisted exfoliation exhibited a dramatic increase in SSA from 30.7 $m^2 \cdot g^{-1}$ (standard delaminated $Ti_3C_2T_x$) to 368.8 $m^2 \cdot g^{-1}$, attributed to interlayer expansion and steric hindrance induced by wrinkled morphology [49]. These findings highlight the critical importance of surface modification, heteroatom doping, and composite design in suppressing restacking and enhancing electrochemical performance. These quantitative insights reinforce the need for systematic material engineering strategies to unlock the full potential of MXene-based composites in practical energy applications.

MXene's surface functional groups (-OH, -F, and -O) have considerable control over its physicochemical properties since these processes modulate hydrophilicity and electrolyte compatibility and serve as active sites for chemical functionalization and composite synthesis [50–53]. In contrast to graphene, which requires chemical doping for high conductivity [54], MXenes are inherently conducive to fast electron transport due to their transition metal-based crystal structure and exhibit higher electrochemical stability compared to MoS_2 [55,56] and other transition metal dichalcogenides [57], supporting stable cycling behavior under varied electrolyte conditions [58,59]. For hydrophobic 2D materials like graphene, MXenes exhibit less surface energy-affected wettability and compatibility with aqueous or polar electrolytes due to surface hydrophilicity. This property, combined with compositional tunability and the ease of integration into polymers and nanoparticles, enables them to be applied to hybrid structures with improved ionic transport and interface contact [60–63].

Several features highlight the advantages of MXenes over other two-dimensional materials. For instance, graphene exhibits extremely high electrical conductivity, with values reaching up to 1×10^6 $S \cdot m^{-1}$, disposed in structured ultrathin films [64]. However, their characteristic lack of surface redox activity and hydrophobic character limit electrochemical performance without further chemical modification. In contrast, $Ti_3C_2T_x$ MXene combines high electrical conductivity (up to ~2×10^6 $S \cdot m^{-1}$) with abundant surface terminations (e.g., -OH, -F, -O) that promote pseudocapacitive charge storage and good interaction with aqueous electrolytes [65]. $Ti_3C_2T_x$ MXene can reach specific capacitance in the order of 400 $F \cdot g^{-1}$, surpassing the typical 100–300 $F \cdot g^{-1}$ observed in MoS_2 and graphene-based electrodes [66,67]. MXenes readily form functional composites with polymers and biopolymers. For example, $Ti_3C_2T_x$ nanosheets decorated with hollow polyaniline nanotubes exhibit enhanced ion accessibility and suppressed restacking [68], while alginate-based MXene composites demonstrate that surface composition directly influences triboelectric behavior and interfacial properties [69]. On the other hand, the overall lamellar structure of MXenes is the reason for their electrochemical activity. Figure 2 shows that the $Ti_3C_2T_x/SnO_2$ composite material possesses a well-defined laminated morphology, evenly stacked MXene layers, and well-dispersed SnO_2 nanoparticles [70]. The low-magnification and high-magnification SEM images (Figure 2a–f) attest to the hierarchical architecture of the composite, where the SnO_2 particles are grafted onto the surface of the $Ti_3C_2T_x$ without disrupting its lamellar network. The HRTEM characterization (Figure 2g,h) confirms the crystal planes of $Ti_3C_2T_x$ and SnO_2 and the measured lattice spacings of 0.925 nm and 0.319 nm, respectively. The resulting SAED pattern (Figure 2i) confirms the coexistence of both phases. Elemental mapping (Figure 2j) shows a uniform distribution of C, O, Ti, Sn, and F throughout the hybrid, confirming the composite structure's homogeneity. Such dual nanostructure facilitates charge transfer, preserves surface accessibility, and enhances the composite's potential sensor and electrochemical applications.

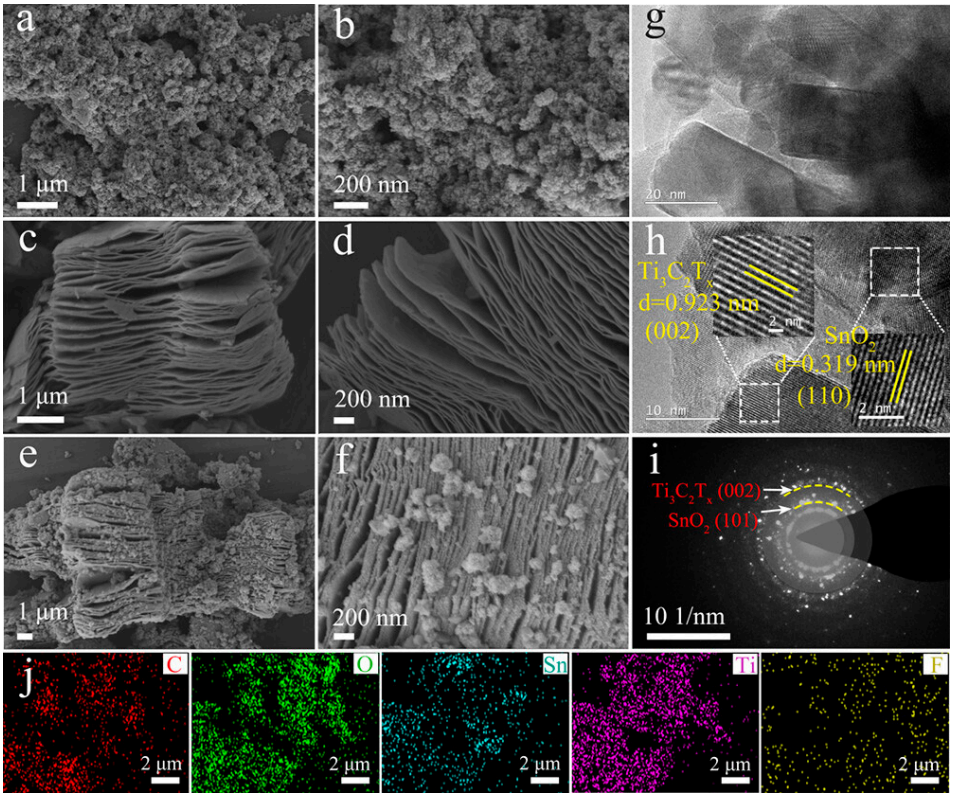


Figure 2. Morphological and structural characterization of $Ti_3C_2T_x/SnO_2$ hybrid. (**a**–**f**) SEM images at various magnifications. (**g**,**h**) HRTEM images. (**i**) SAED pattern. (**j**) Elemental mapping. Reprinted with permission from Ref. [70]. Copyright 2024 American Chemical Society.

The growing demand for high-performance batteries and supercapacitors has driven the development of MXene-based hybrid formulations, incorporating conducting polymers, carbon nanostructures, and metal oxides to enhance electrochemical performance and cycling durability [31,71,72].

One of the most extensively studied MXenes is $Ti_3C_2T_x$, which exhibits good specific capacitance and electrochemical stability. The surface functional groups, such as -O, -F, and -OH, can control electrochemical behavior by enhancing electrolyte affinity and efficient interfacial charge transfer. For instance, -OH groups enable hydrogen bonding between electrolyte molecules, facilitating lower interfacial resistance and enhanced ionic diffusion [73–75]. Similar benefits have been reported for $Mo_2TiC_2T_X$ [76] and $V_4C_3T_X$ [77–79], which exhibit enhanced redox activity and high specific capacity in lithium and sodium-ion batteries, particularly in aqueous systems [80–84]. Other MXenes, such as $Mo_4VC_4T_x$ [85,86], Ti_2C [87,88], Nb_2C [89], and TiVC [90,91], introduce complementary advantages relative to multivalent redox behavior, high conductivity, and structural tunability, improving the applicability in electrolytic media [92]. Their ability to support diverse intercalation groups makes them adaptable for capacitive and faradaic energy storage mechanisms.

This review aims to present a general overview of the development and application of MXenes and their composites in energy storage, sensors, and hybrid devices being focused on major strategies for performance enhancement—i.e., synthesis, structural tailoring, and integration with other nanomaterials. This study highlights principal challenges that limit industrialization, outlining the function ascribed to MXene-based devices, namely, versatile, cutting-edge applications for future energy and electronics.

2. Strategies for Improvement in the Electrochemical Performance of MXene

An essential feature that enables performance optimization in MXenes is their functional surface, typically terminated with groups such as -OH, -F, -O, or -Cl. These groups influence hydrophilicity, interfacial compatibility, redox activity, and charge transport, playing a pivotal role in modulating the MXene/electrolyte interaction, reducing interfacial resistance, and enhancing ion mobility.

However, MXenes are chemically unstable under ambient conditions in oxidative processes often initiated by exposure to water or oxygen, which can significantly degrade their conductivity and electrochemical properties, ultimately compromising device cyclability. Mitigation strategies include inert-atmosphere storage, protective coatings, and functional surface passivation. Chemical modification with chloride or sulfonate groups enhances thermal and oxidative stability while improving ionic conductivity, especially for application in membranes and hybrid electrolytes [93–95]. MXene nanosheet restacking represents a critical limitation, as the layered structures tend to collapse upon drying or cycling, consequently reducing the accessible surface area, hindering ion diffusion, and compromising active material utilization in energy storage devices. As a result, researchers have introduced various interlayer spacers, including carbon nanotubes, polymers, metal oxides, or fullerenes [63,68,96].

Synthesis routes significantly impact MXene morphology, purity, and functionality. The most common method involves the selective etching of the A element from MAX phases using hydrofluoric acid (HF) or in situ HF generated via an HCl and LiF mixture. Despite being effective, these routes raise environmental and safety concerns. Recent efforts have explored alternative strategies such as electrochemical etching, molten salt synthesis, and mechanical exfoliation to enhance safety, process control, and sustainability. For instance, pre-washing with $NaHCO_3$ or using Lewis acidic molten salts such as $ZnCl_2$ during etching has enabled the production of Cl-terminated MXenes with improved cycling stability and thermal resistance [97–99].

As illustrated in Figure 3, Ma et al. proved that it is possible to regulate different synthesis routes to effectively regulate MXene surface terminations through molten salt treatment with $CuCl_2$ and Li_2O. In contrast to conventional HCl/LiF etching, which results in mainly F-terminated MXenes, the chemical treatment enables the formation of Cl-terminated and, finally, O-terminated Ti_3C_2 structures. SEM and elemental mapping images (Figure 3b–d) confirm the successful incorporation and homogeneous dispersion of the desired surface terminations, while freestanding membrane images (Figure 3e–h) show morphological differences and the structural compatibility of these surface-modified MXenes with flexible substrates. These observations demonstrate the potential capability of post-synthetic thermal treatments to enhance the surface chemistry of MXene, thereby improving its electrochemical stability and performance [100].

An additional critical aspect is the integration of MXenes into device architectures, where their use in thin films, coatings, and electrodes demands strong adhesion to substrates. Techniques such as electrodeposition and self-assembly facilitate the formation of uniform layers [101,102]. This process enhances mechanical durability and maintains electrical performance during repeated cycling and bending, which is essential for developing flexible and wearable energy devices. The choice of electrolyte plays a crucial role in determining the performance of MXene-based devices. Aqueous electrolytes exhibit high ionic conductivity but suffer from a narrow electrochemical stability window, limiting the potential voltage output. On the other hand, organic solvents such as acetonitrile, dimethyl sulfoxide, and propylene carbonate, when paired with salts such as LiTFSI, offer voltage windows up to 2.4 V. Furthermore, ionic liquids extend the window to approximately 3.0 V, with improved energy and power density, while maintaining long-term

device stability [103–106], minimizing side reactions, and improving electrolyte–electrode compatibility [20].

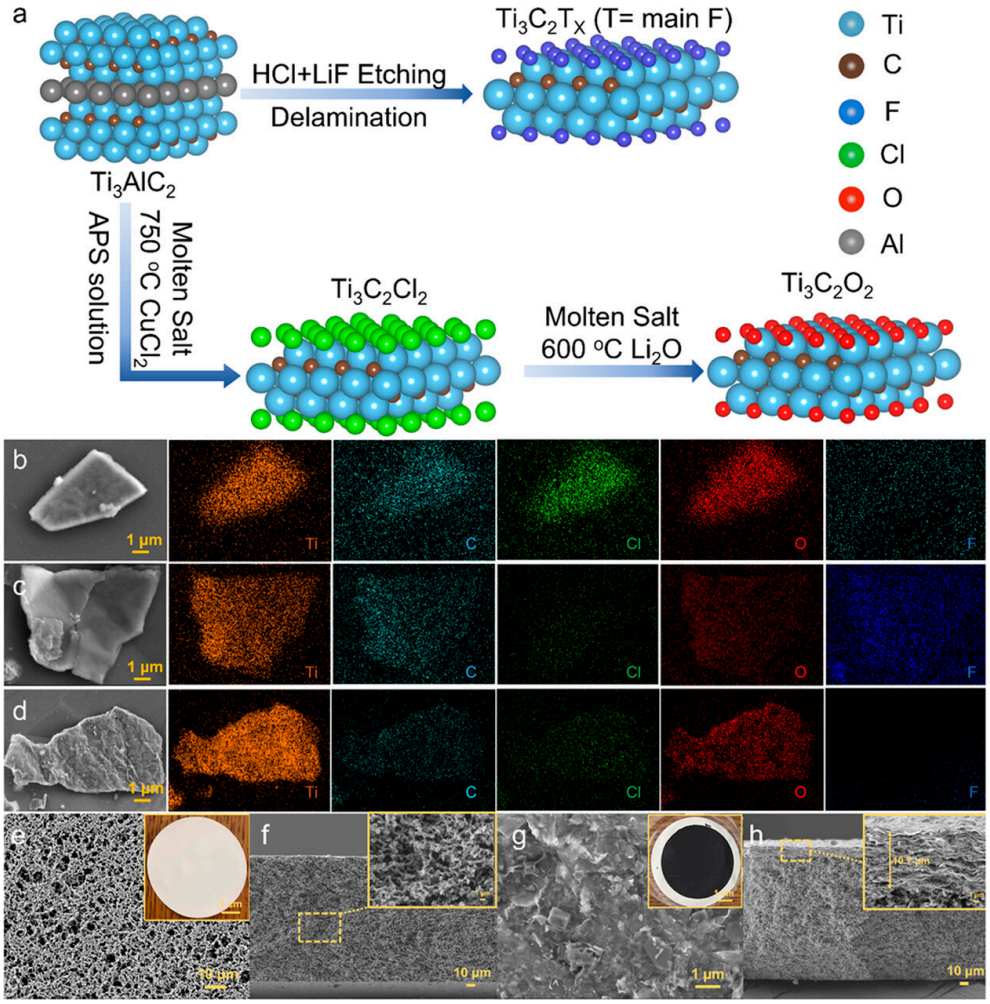


Figure 3. Synthesis and characterization of surface-terminated MXenes. (**a**) Schematic of $Ti_3C_2T_x$ synthesis. (**b**–**d**) SEM and elemental mapping confirm incorporation of surface terminations. (**e**–**h**) SEM images of freestanding MXene membranes with different terminations. Reprinted with permission from Ref. [100]. Copyright 2023 American Chemical Society.

Developing flexible and wearable technologies has increased interest in solid and quasi-solid-state electrolytes. Incorporating MXenes into polymer matrices, such as solid polymer electrolytes (SPEs) and MXene-hydrogel hybrids, improves ionic conductivity, thermal stability, and mechanical flexibility [107,108]—with special interest in zinc-ion and lithium-ion batteries—by overcoming key challenges such as dendrite growth and poor interfacial stability, while enabling the design of safe and lightweight architectures [109–111].

2.1. MXene Composites for Supercapacitors and Batteries

The intrinsic metallic conductivity of MXenes allows rapid charge transfer, while their layered structure provides efficient ion diffusion pathways, resulting in high power density and excellent cycling stability in supercapacitors. Similarly, batteries' enhanced rate capability and reversible capacity are attributed to fast electron transport and the abundance of active surface sites for redox reactions.

Limited interlayer spacing could also restrict electrolyte penetration, affecting electrochemical performance [96]. Consequently, MXene-based composites enable the development of enhanced architectures that maintain optimized electrical, ionic, and mechanical

properties. This results in supercapacitors with greater specific capacitance and energy density and batteries with higher capacity retention, fast charge–discharge rates, and extended cycling life [27,112–114]. The potential and limitations of composites are discussed as follows.

2.1.1. MXene + Conducting Polymers Composites

The MXene/conducting polymer composites combine the high conductivity of MXenes with the redox activity and mechanical flexibility of conducting polymers such as polyaniline (PANI) and PEDOT:PSS [115,116], resulting in improvements in specific capacitance, cycling stability, and electrode integrity. MXene surface functional groups enable uniform polymer deposition and strong interfacial bonding, facilitating charge transport and mechanical adhesion [117,118]. Composite synthesis methods, such as in situ polymerization, solution blending, and layer-by-layer assembly, are crucial in defining morphology and performance. Specifically, in situ polymerization enables the homogeneous coating of polymers onto MXene flakes, optimizing electron/ion transport and preserving mechanical stability in cyclic conditions [119–121]. The resulting composites can be processed into flexible films, fibers, or coatings, making them highly promising for wearable and deformable electronics applications [27,122]. However, preventing sheet restacking and preserving long-term polymer stability remain difficult. Strategies such as the use of interlayer spacers and electrostatic repulsion through surface modification have been employed to maintain expanded lamellar structures. Furthermore, selecting redox-stable polymers and optimizing synthesis parameters are key to ensuring durability during prolonged cycling [118,119,121,123].

As shown in Figure 4, Liu et al. demonstrated the synthesis of sulfonated $Ti_3C_2T_x$ (S-$Ti_3C_2T_x$) and the incorporation of PANI to form a high-performance composite. The presence of sulfonic acid groups on the MXene surface enables strong electrostatic and hydrogen bonding interactions with the polymer chains, stabilizing the PANI network and enhancing electrochemical cyclability. This interfacial interaction promotes enhanced ionic transport and charge retention under repeated cycling conditions, highlighting the synergistic advantages of surface-functionalized MXene–polymer composites in energy storage systems [124].

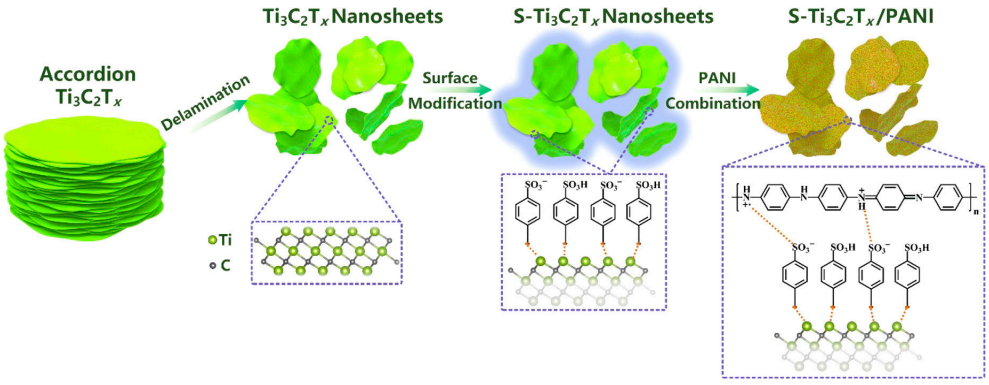


Figure 4. Schematic representation of synthesis and functionalization pathway for S-$Ti_3C_2T_x$/PANI composites. Reprinted with permission from Ref. [124]. Copyright 2021 American Chemical Society.

Consequently, the S-$Ti_3C_2T_x$/PANI composite realized a high reversible capacity of 262 mAh g^{-1} at 0.5 A g^{-1}, which remained 160 mAh g^{-1} at 15 A g^{-1}, achieving 100% Coulombic efficiency after 5000 cycles. Importantly, the Zn-ion battery using this cathode preserved 61.1% of energy at a power density of 15,500 W kg^{-1}, far exceeding the values of common electrode materials, which usually remain below 50% under similar conditions. These results highlight the strategic importance of MXene surface functionalization

in enhancing rate capability and energy retention in high-performance energy storage devices [124].

2.1.2. MXene + Carbon Derivative Nanomaterials

MXenes and CNTs/graphene composites offer a path toward flexible, high-surface-area, and mechanically robust electrodes [125,126]. The disposition of CNTs between MXene layers effectively suppresses sheet restacking and enhances electrical conductivity [127]. These hybrids demonstrate high specific capacitance, rate capability, and cycling performance. Graphene-based composites improve flexibility and energy density, making them suitable for flexible supercapacitors and hybrid batteries [128–130]. MXene–carbon composites enhance sensitivity and selectivity in sensing applications, enabling the accurate detection of gases and biomolecules in wearable and biomedical devices [127,131].

Standard synthesis methods include vacuum filtration, electrostatic self-assembly, and solution mixing, which allow the scalable production of homogeneous composites. Tuning the MXene-to-carbon ratio and optimizing interfacial interactions are critical for tailoring performance to specific device requirements [132–134]. Future research efforts must prioritize surface engineering and the development of advanced synthesis techniques to overcome these challenges and broaden the application scope [135,136].

Shi et al. reported that the incorporation of CNTs into $Ti_3C_2T_x$ MXene films increased the specific surface area, as illustrated in Figure 5, in which the CNT content varied from 60 wt% to 90 wt% and induced a significant reduction in the lamellar thickness of MXene-CNT composite films. The SEM images reveal that CNTs are highly dispersed among MXene layers, serving as spacers that ensure there is a layered architecture and enhance the ion-accessible surface area. This structure's engineering enhances ionic diffusion channels, mechanical strength, and electrode flexibility, positioning MXene carbon nanocomposites as the material of choice for flexible and high-rate energy storage devices. The $Ti_3C_2T_x$ MXene film's surface area was increased from approximately 18 $m^2\ g^{-1}$ (pristine) to over 52 $m^2\ g^{-1}$ in a composite containing 90 wt% CNT without losing structural alignment and electrical conductivity, enhancing ion accessibility and allowing for efficient charge transfer. Moreover, nitrogen adsorption–desorption measurements confirmed an increase in total pore volume and mesoporosity development, resulting from CNT insertion, which is essential for promoting fast ionic transport. These hybrids demonstrate high specific capacitance, rate capability, and cycling performance. The composite containing 80 wt% MXene had a very high specific capacitance of 318 F g^{-1} at 1 A g^{-1} and retained 165 F g^{-1} at 20 A g^{-1}, demonstrating over 50% capacitance retention and exhibiting excellent rate capability. The electrode also possessed excellent cycling stability, retaining 98% of the initial capacitance after repeated 5000 cycles of charge–discharge at a high current density of 20 A g^{-1}. These results highlight the role of CNTs as effective spacers that suppress the restacking of MXene sheets and preserve ion-accessible surface area, leading to structurally stable and high-performance electrodes [128].

2.1.3. MXene + Metal Oxides and Ceramics Composites

Combining MXenes with metal oxides and ceramics potentializes the components' electrical conductivity, redox activity, and mechanical robustness [137–139], improving capacitance and cyclic stability due to the pseudocapacitive behavior of oxides such as MnO_2, TiO_2, and CoO anchored to conductive MXene matrices [37,140–142], with MXene enhancing thermal conductivity, mechanical strength, and electromagnetic shielding in ceramic matrices. These composites are well-suited for high-temperature environments and applications that require energy storage and simultaneous thermal management [143,144]. MXene-oxide hybrids demonstrate high selectivity for gas and biomolecule detection

due to their modifiable surface chemistry and synergistic interfacial interactions [145,146]. Solvothermal synthesis, chemical deposition, and self-assembly approaches are commonly used to fabricate these materials [137,145]. As with other hybrids, scale-up and long-term stability are key challenges. Efforts in interfacial engineering, oxidation mitigation, and morphology control continue to drive research progress toward achieving consistent and reliable performance in MXene-based systems [70,147].

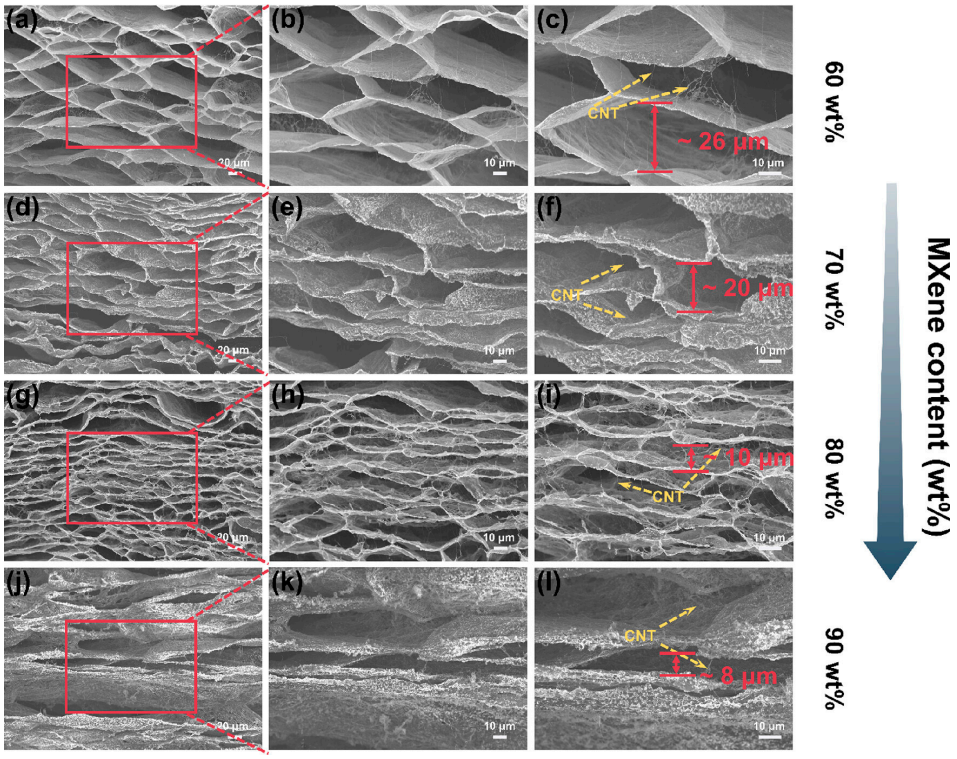


Figure 5. Cross-sectional SEM images of MXene/CNT composite films with varying MXene contents (60–90 wt%). (**a**–**c**) 60 wt%, (**d**–**f**) 70 wt%, (**g**–**i**) 80 wt%, and (**j**–**l**) 90 wt%. CNTs act as interlamellar spacers between MXene nanosheets, reducing film thickness from ~26 µm to ~8 µm. Reprinted with permission from Ref. [128]. Copyright 2023 American Chemical Society.

Incorporating redox-active metal oxides into MXene frameworks combines the electrical double-layer capacitance (EDLC) of MXene sheets with the faradaic pseudocapacitance provided by the oxides. Within CuO/MXene nanocomposites, dispersed CuO nanoparticles are redox-rich sites with reversible Cu^{2+}/Cu^{+} redox transitions that significantly enhance the charge storage capacity. In addition, the highly conductive $Ti_3C_2T_x$ matrix delivers quick electron transfer across the electrode and enables effective charge redistribution during cycling. This configuration also introduces accessible ion diffusion channels in the layer structure, further enhancing electrochemical kinetics. As evident from Figure 6, the CuO/MXene nanocomposite exhibits a homogeneous CuO phase uniformly and evenly anchored on $Ti_3C_2T_x$ nanosheets, forming a well-structured electrode. SEM images show CuO nanoparticles densely clustered on MXene's surface, and EDS analysis confirms the presence of Ti, Cu, O, and C, along with even dispersion. This architecture increases the number of active redox sites and boosts electrical conductivity through close interface contact. Galvanostatic charge–discharge (GCD) measurements revealed that the CuO@βCD/MXene (1:1) composite exhibited superior pseudocapacitive behavior, with a specific capacitance of approximately 1693 F g^{-1} at 0.9 A g^{-1}, significantly higher than that of pristine MXene (around 1125 F g^{-1}) or CuO@βCD (about 582 F g^{-1}) under the same conditions. The composite retained its capacitance, even at higher current densities, confirming its excellent rate capability. In addition, the 1:1 electrode preserved 94% of its initial capacitance after 5000 cy-

cles at 10 A g^{-1}. Moreover, the device achieved a specific energy of 28.5 Wh kg^{-1} and a power density of 750 W kg^{-1}, confirming the synergistic interaction between MXene and CuO in delivering both high energy density and long-term electrochemical stability [148].

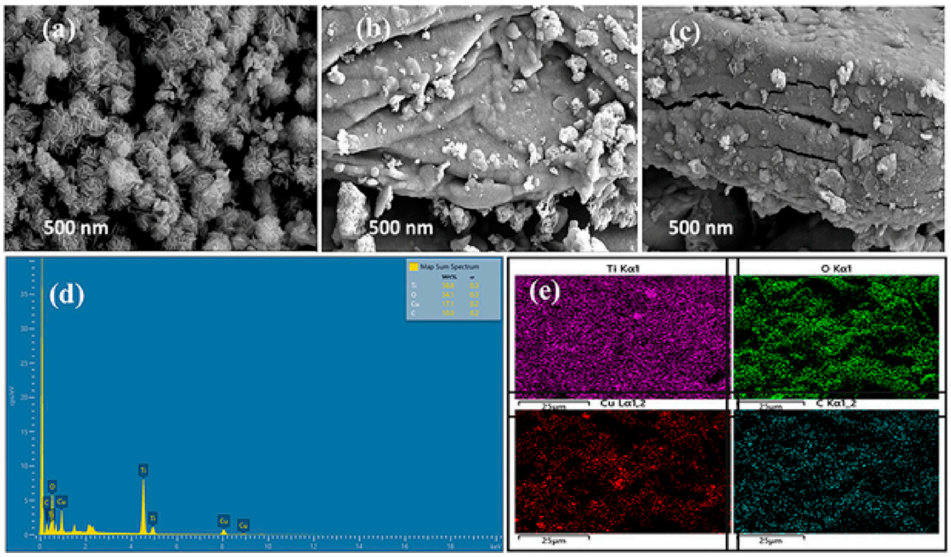


Figure 6. Structural and compositional characterization of CuO/MXene nanocomposite electrode. (**a**–**c**) SEM images at different magnifications; (**d**) EDS spectrum; (**e**) elemental mapping of Ti, O, Cu, and C. Reprinted with permission from Ref. [148]. Copyright 2023 American Chemical Society.

3. Hybrid Applications of MXene-Based Composites

MXene-based composites achieve superior performance in energy storage, sensing, and energy harvesting applications through the synergy of structural, chemical, and interfacial mechanisms. The high electrical conductivity and open lamellar structure of MXenes (e.g., $Ti_3C_2T_x$), facilitating efficient electron transport and ion intercalation, are the main properties for charge storage in energy devices. Their capacitive performance arises from electrical double-layer capacitance (EDLC) and pseudocapacitance. Surface terminations (-OH, -O, -F) modulate redox activity and electrolyte compatibility, improving charge transfer and rate performance [34,149]. Hybridization with redox-active components such as transition metal oxides (e.g., VS_2, CuO) or conductive polymers (e.g., PANI) further boosts storage by introducing faradaic processes and suppressing the restacking of MXene sheets. As a representative case, VS_2/MXene electrodes showed over 90% surface-controlled pseudocapacitive contribution, enhancing specific capacitance and voltage window [150,151]. MXene composites operate through piezoresistive or ionic conduction mechanisms in sensing applications. In strain and pressure sensors, mechanical deformation alters the conductive pathways between MXene flakes or within a hydrogel matrix, leading to changes in electrical resistance [152]. MXene–polymer hydrogels also support ionic conduction, where the deformation-induced reorganization of hydrogen bonding networks modulates ion mobility [153]. Integrating cellulose nanofibers (CNFs) and MXene into polyacrylamide hydrogels enables a gauge factor of ~6.7 and response times below 110 ms [154]. In gas sensors, MXene surfaces adsorb analytes directly, altering surface conductivity [155]. Functionalization with polymers such as p(PFDMA) improves selectivity and reversibility by facilitating gas diffusion and controlling adsorption kinetics [95].

For triboelectric nanogenerators (TENGs), MXenes function as electrodes or active triboelectric layers. Their lamellar morphology ensures conformal contact with dielectrics like PDMS or alginate, while surface groups (-OH, -F) influence charge transfer direction and triboelectric polarity [27,156]. Moreover, interfacial interactions, particularly hydrogen bonding between MXene and biopolymers, enhance dipole alignment and surface charge

density. For example, Ti_3CN-based composites generate higher triboelectric outputs than Ti_3C_2 due to more abundant surface functionalities, promoting stronger bonding [27]. In multifunctional hydrogels, MXene also enables the development of hybrid sensing mechanisms by combining ionic conduction (through salt-induced ion migration) and triboelectric charge generation, enabling their use in multifunctional self-powered strain sensors [152]. These synergistic mechanisms across structural, electrical, and interfacial levels make MXene-based composites ideal candidates for multifunctional, high-performance energy, and sensing devices.

3.1. MXenes in Hybrid Energy Storage Devices

Energy storage technologies are typically divided into four forms: symmetric supercapacitors, asymmetric supercapacitors, hybrid supercapacitors (also known as supercapatteries), and batteries. The most distinctive difference among these systems lies in the charge storage mechanisms. Symmetric supercapacitors employ identical electrodes, typically composed of materials possessing electric double-layer capacitance (EDLC) properties, where energy is stored by the separation of electrostatic charges at the electrode/electrolyte interface [157]. Conversely, asymmetric supercapacitors pair a capacitive (EDLC-type) electrode with a pseudocapacitive one that experiences surface redox reactions, enabling a wider voltage window and greater energy density [81]. Hybrid supercapacitors (supercapatteries) combine a pseudocapacitive electrode with a battery-type electrode to bridge supercapacitors' high power density with a battery's high energy density, resulting in devices that deliver intermediate but highly efficient performances [150]. In contrast, traditional batteries only employ faradaic bulk processes involving ion intercalation, which enables high energy density, but often at the expense of power density and cycle life [158].

In this context, MXenes have been recognized as strategic materials. Their lamellar structure, excellent electrical conductivity, and tunable surface chemistry enable the formation of superior electrochemical response electrodes. The combination of MXenes with metal oxides [37], conducting polymers [124], carbon materials [128], or MOF structures [159] has led to the formation of optimized hybrid structures appropriate for supercapacitors and rechargeable batteries, including lithium-, sodium-, and zinc-ion systems. Integrating these elements avoids the limitations of individual components, confers significant improvements in the specific capacitance, energy density, and cycling stability, and becomes a crucial element of future energy storage devices.

3.1.1. MXene-Based Hybrid Supercapacitors

As shown in Table 1, essential advances have been achieved in developing MXene-based hybrid supercapacitors, particularly through morphological control, electrolyte selection, and integration with redox-active or conductive materials that exhibit outstanding performance in interactions with transition metal dichalcogenides.

The VSe_2/e-MXene/CNT//AC composite is a 3D hybrid structure used for high-stability and high-power applications. Redox-active vanadium diselenide (VSe_2) is employed on the positive electrode in combination with electrochemically modified MXene (e-MXene), which is connected by carbon nanotubes. The CNTs enhance the electrical conductivity by adding an intermixed porous structure, preventing MXene restacking and enabling easy ion and electron transfer with the activated carbon negative electrode. A 0.5 M K_2SO_4 electrolyte was used, resulting in a capacitance of 101 F g^{-1} at 1.6 A g^{-1}, an energy density of 35.91 Wh kg^{-1}, a power density of 1280 W kg^{-1} at 1.6 V, and 99% capacitance retention after 5000 cycles [151]. The VS2–MXene composite electrode has significantly better electrochemical properties than either individual component. The hybrid displays higher specific capacitance, increased capacitive charge storage contribution, and a broader

operational voltage window, arising from the synergistic interaction between the high conductivity and layered structure of MXene and the redox-active nature of VS_2. The electrochemical performance of VS_2/MXene electrodes is well-documented, as shown in Figure 7. Figure 7a illustrates the specific capacitance values versus current density, where the composites excel over pristine VS2 and MXene separately, with the best compromise between capacitance and rate capability achieved by 50% hybrids (VS2–MXene–50). Figure 7b is a cyclic voltammetry (CV) plot of the hybrid at 30 mV s^{-1} and shows a capacitive contribution of 92.1%, confirming its predominantly surface-controlled charge storage behavior. Figure 7c is a capacitive and diffusion-controlled contributions plot at various scan rates, where capacitive effects still predominate at 50 mV s^{-1}. Figure 7d compares CV profiles of pristine MXene and the VS2–MXene hybrid at 30 mV/s, revealing the much larger integrated area and better pseudocapacitive performance of the hybrid. Figure 7e presents CV plots of the VS2–MXene device across voltage windows (1.4–1.8 V), demonstrating stable and broad electrochemical operation. Figure 7f shows galvanostatic charge–discharge (GCD) responses at 5 A g^{-1}. The response is characterized by a symmetric and extended charge–discharge cycle, characterizing a high-efficiency hybrid storage. The system demonstrates the potential of MXene-based hybrids for use as high-energy, high-rate asymmetric supercapacitors [150].

The GeOx@$Ti_3C_2T_x$//AC hybrid supercapacitor contains GeOx nanospheres surface-attached onto $Ti_3C_2T_x$ MXene sheets through hydrothermal synthesis and further ultrasonic dispersion. In this arrangement, the positive electrode, formed by the GeOx/MXene heterostructure, exhibits pseudocapacitive behavior associated with reversible redox reactions of the Ge^{4+}/Ge^{2+} redox couple, enhancing the charge storage capability. In contrast, the AC-based negative electrode offers a high surface area, along with EDLC behavior, which is responsible for the device's total energy storage performance. The system operates in an aqueous 1 M $(NH_4)_2SO_4$ electrolyte to provide electrochemical stability and ionic conductivity. The 2D/0D lamellar structure promotes effective ion diffusion and structural integrity. The device achieved 141 F g^{-1} at 1 A g^{-1}, with a 51.4 Wh kg^{-1} energy density at 1.6 V. Interestingly, capacitance retention was 92.6% at 20 A g^{-1} after 10,000 cycles, indicating high-quality electrochemical stability [147].

In the MXene-NPO//PPD-rGO system, the hybrid structure combines a positive electrode of MXene, functionalized with nickel phosphate (NPO), with a negative electrode of polypyrrolidone-functionalized reduced graphene oxide (PPD-rGO). The device employs a PVA/KOH gel electrolyte, making it suitable for solid and flexible devices. The interaction between components ensures high conductivity and ion accessibility. This configuration delivered 187 F g^{-1} at 1 A g^{-1}, 72.6 Wh kg^{-1} energy density, and 932 W kg^{-1} power density at 1.6 V, maintaining 94% capacitance after 10,000 cycles [159].

The MXene//AC-Nafion system is a high-performance asymmetric supercapacitor that uses a negative electrode of Nafion-functionalized activated carbon and a positive electrode of $Ti_3C_2T_x$ MXene. Nafion—a sulfonated perfluorinated polymer with $–SO_3H$ groups—enhances proton conductivity and thermal stability, improving ion mobility and structural integrity. Operating in 3 M H_2SO_4, the device reached 555 F g^{-1} at 1 A g^{-1}, an energy density of 81.2 Wh kg^{-1}, and a power density of 1023 W kg^{-1}, with 93% retention after 5000 cycles at 2.0 V [160].

A urea-assisted nitrogen-doped UN-$Ti_3C_2T_x$ symmetric supercapacitor was designed to prevent MXene restacking, which inhibits ion diffusion. Nitrogen doping was combined with chemical delamination, using urea as the nitrogen source. This had the effects of incorporating $–NH_2$ and –N= functional groups, expanding the interlayer distance, and improving electrolyte access and structural stability. The device operates with an organic

electrolyte (1 M EMIMTFSI/LiTFSI in acetonitrile), which allows a wide voltage window of 2.4 V and a specific capacitance of 147 F g^{-1} at 0.5 A g^{-1} [104].

The Ni-MOF/MXene composite supercapacitor was developed via a folic acid-assisted solvothermal route, via the in situ deposition of nickel-based MOF nanosheets on $Ti_3C_2T_x$ layers. The hybrid porous structure increases the surface area and creates rich redox-active Ni^{2+}/Ni^{3+} sites. The device, with an activated carbon (AC) counter-electrode and aqueous 1 M KOH electrolyte, achieved 716.2 F g^{-1} at 1 A g^{-1}, an energy density of 23.28 Wh kg^{-1}, and a power of 2841 W kg^{-1}, operating at 1.5 V with 74.2% retention after 2000 cycles [161].

An asymmetric solid-state configuration of a 3D hierarchical MXene/WO_3 nanorods/rGO sponge and porous carbon was developed. In this structure, WO_3 nanorods were deposited on the MXene and reduced graphene oxide (rGO) composite matrix, with an effective balance of electrical conductivity, pseudocapacitive storage, and mechanical strength. Operated with a PVA gel electrolyte containing 2 M KOH and 0.1 M $K_4[Fe(CN)_6]$, the device delivered 123.4 F g^{-1} at 2 A g^{-1}, 34 Wh kg^{-1} energy, 1450 W kg^{-1} power, and 86% retention over 3000 cycles [108].

An asymmetric supercapacitor with a 2D MXene/NiCoP hybrid as the positive electrode and ZIF-derived porous carbon as the negative electrode exhibited superior electrochemical behavior. The MXene decorated with NiCoP, in combination with this device, provided excellent redox activity and structural stability, while the ZIF-8-derived carbon framework ensured complementary conductivity and capacitive characteristics. It operated with 2 M KOH, 1754 F g^{-1} at 3 mA cm^{-2}, an energy density of 54.3 Wh kg^{-1}, a power of 565.6 W kg^{-1} at 1.6 V, and a 93.8% capacity retention over 10,000 cycles [162].

A flexible solid-state supercapacitor composed of a 3D network porous MXene/carbon dot film (p-MC) used an NH_3-induced etching process to produce expanded interlayer spaces and porosity. Under operation with a PVA/H_2SO_4 gel electrolyte, the system returned a specific capacitance of 688.9 F g^{-1} at 2 A g^{-1}, energy density of 20 Wh kg^{-1}, 600 W kg^{-1} of power, and 90% of retention after 10,000 cycles [163].

A different symmetric all-solid-state supercapacitor made of PLA/PANI/MXene (PPM) composite was prepared via the in situ polymerization of polyaniline onto a polylactic acid matrix incorporating MXene sheets. The PVA/H_2SO_4 gel electrolyte provided mechanical and electrochemical stability. The device delivered 193.7 F g^{-1} at 0.25 A g^{-1}, 9.3 Wh kg^{-1} energy density, 291.3 W kg^{-1} power, and 80.3% retention after 5000 cycles under a 0.6 V voltage window [164].

A PANI/MXene supramolecularly optimized device functionalized by a cyclodextrin polymer (CDP-MX/PA) showed an outstanding performance. Cyclodextrin facilitated homogeneous PANI growth, reduced aggregation, and preserved the MXene layer spacing. Operating in 1 M H_2SO_4, the device delivered 523.8 F g^{-1} at 1 A g^{-1}, an energy density of 27.7 Wh kg^{-1}, 700 W kg^{-1} power, 1.4 V, and 86.5% retention after 5000 cycles [118].

The asymmetric supercapacitor extracted from 2D MXene-PVP-Co_9S_8//MoS_2 composition consists of Co_9S_8 nanoparticles that are anchored onto PVP-functionalized MXene as the positive electrode, while MoS_2 serves as the negative electrode. Synthesized by a hydrothermal route and examined in 6 M KOH, the system delivered a specific capacitance of 277 F g^{-1} at 1 A g^{-1}, an energy density of 111 Wh kg^{-1} energy, a power density of 845 W kg^{-1} power, and a working voltage of 1.7 V, with a 84% capacitance retention after 10,000 cycles [165].

Lastly, the MXene-NPO//AC system is a flexible asymmetric solid-state supercapacitor with in situ phosphorized Ni-MOF nanorods grown on MXene as the positive electrode and activated carbon as the negative electrode. Assembled in a PVA/KOH gel electrolyte, the device achieved 332 F g^{-1} at 1 A g^{-1}, 118 Wh kg^{-1} energy density, 799.7 W kg^{-1} power, 1.6 V, and 99.7% retention after 1000 cycles [166].

Table 1. Electrochemical Performance of MXene-Based Supercapacitors.

Structure	Device	Electrolyte	Specific Capacitance	Energy Density $Wh \cdot kg^{-1}$	Power Density $W \cdot kg^{-1}$	Voltage Window	Capacitance Retention	Ref.
GeOx@$Ti_3C_2T_x$//AC	Hybrid Supercapacitor	1 M $(NH_4)_2SO_4$ (aqueous)	141 $F \cdot g^{-1}$ at 1 $A \cdot g^{-1}$	51.4	800.6	1.6 V	92.6% at 20 $A \cdot g^{-1}$ after 10,000 cycles	[147]
MXene-NPO//PPD-rGO	Hybrid Supercapacitor	KOH/PVA gel	187 $F \cdot g^{-1}$ at 1 $A \cdot g^{-1}$	72.6	932	1.6 V	94% after 10,000 cycles	[159]
MXene//AC-Nafion	Asymmetric Supercapacitor	3 M H_2SO_4	555 $F \cdot g^{-1}$ at 1 $A \cdot g^{-1}$	81.2	1023	2 V	93% after 5000 cycles at 1 $A \cdot g^{-1}$	[160]
N-doped $Ti_3C_2T_x$ (UN-$Ti_3C_2T_x$)	Symmetric Supercapacitor	1 M EMIMTFSI/LiTFSI in ACN	147 $F \cdot g^{-1}$ at 0.5 $A \cdot g^{-1}$	29.4	600	2.4 V	-	[104]
VSe_2/e-MXene/CNT	Asymmetric Supercapacitor	0.5 M K_2SO_4 (aqueous)	101 $F \cdot g^{-1}$ at 1.6 $A \cdot g^{-1}$	35.91	1280	1.6 V	~99% after 5000 cycles	[151]
Ni-MOF/MXene Composite	Hybrid Supercapacitor	1 M KOH (aqueous)	716.19 $F \cdot g^{-1}$ at 1 $A \cdot g^{-1}$	23.28	2,841	1.5 V	74.22% after 2000 cycles	[161]
MXene-WO_3 nanorods–rGOsp//Porous carbon	Asymmetric Supercapacitor	PVA gel + 2 M KOH + 0.1 M $K_4[Fe(CN)_6]$	123.4 $F \cdot g^{-1}$ at 2 $A \cdot g^{-1}$	34	1450	1.45 V	86% after 3000 cycles at 5 $A \cdot g^{-1}$	[108]
2D MXene/NiCoP + ZIF-derived porous carbon	Asymmetric Supercapacitor	2 M KOH (aqueous)	1754.0 $F \cdot g^{-1}$ at 3 $mA \cdot cm^{-2}$	54.3	565.6	1.6 V	93.8% after 10,000 cycles 20 $mA \cdot cm^{-2}$	[162]
3D-interconnected porous MXene/carbon dot film (p-MC)	Flexible All-Solid-State Supercapacitor	PVA/H_2SO_4 gel	688.9 $F \cdot g^{-1}$ at 2 $A \cdot g^{-1}$	20	600	1.2 V	90% after 10,000 cycles 8 $A \cdot g^{-1}$	[163]
PLA/PANI/MXene (PPM) Composite	Symmetric Supercapacitor	1 M PVA/H_2SO_4 gel	193.7 $F \cdot g^{-1}$ at 0.25 $A \cdot g^{-1}$	9.3	291.3	0.6 V	80.3% 5000 cycles at 2 $A \cdot g^{-1}$	[164]
CDP-MX/PA (PANI/MXene + cyclodextrin polymer)	High-Performance Supercapacitor	1 M H_2SO_4	523.8 $F \cdot g^{-1}$ at 1 $A \cdot g^{-1}$	27.7	700	1.4 V	86.5% 5000 cycles at 5 $A \cdot g^{-1}$	[118]
2D MXene-PVP-Co_9S_8//MoS_2	Hybrid Supercapacitor	6 M KOH	277 $F \cdot g^{-1}$ at 1 $A \cdot g^{-1}$	111	845	1.7 V	84% 10,000 cycles at 10 $A \cdot g^{-1}$	[165]
MXene-NPO//AC	Asymmetric Supercapacitor	PVA/KOH gel	332 $F \cdot g^{-1}$ at 1 $A \cdot g^{-1}$	118	799.7	1.6 V	99.7% to 95.1% at 5 $A \cdot g^{-1}$ for 1000 cycles	[166]

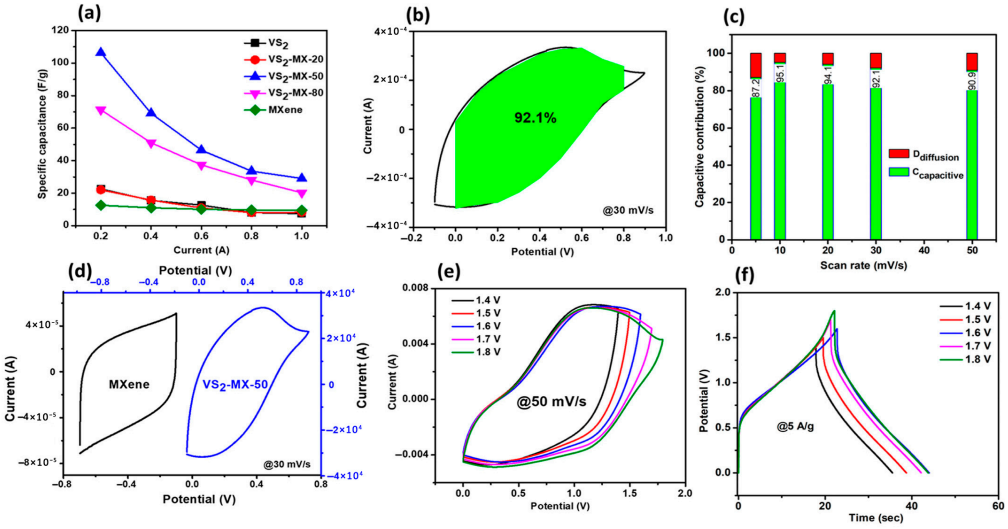


Figure 7. Electrochemical performance of VS_2/MXene hybrid electrodes for asymmetric supercapacitors. (**a**) Specific capacitance vs. current (**b**) Capacitive contribution analysis. (**c**) Contribution at different scan rates. (**d**) CV curves of MXene and VS_2–MXene at 30 mV/s. (**e**) CV of the assembled device at various voltage windows. (**f**) GCD profiles at 5 A g^{-1}. Adapted with permission from Ref. [150]. Copyright 2021 American Chemical Society.

3.1.2. MXenes as Electrodes in Batteries

The high electrical conductivity, layered structure, and ability of MXene-based systems to be functionalized with polymers, oxides, or metals make them well-suited for various battery systems, including lithium-, sodium-, and zinc-ion, as well as lithium–sulfur, chemistries. An example includes the $Ti_3C_2T_x$//$FeVO_4$ (2:1) electrode structure that combines MXene sheets with iron vanadate ($FeVO_4$) in a 2:1 ratio to create an electrode with very high redox-active sites and a structurally complementary conductive lamellar framework. This interaction facilitates effective Li+ insertion and extraction, thereby stabilizing the cycling process. The cell utilizes $LiPF_6$ in a mixture of ethylene carbonate (EC) and dimethyl carbonate (DMC) as the electrolyte, which is characterized by its high electrochemical stability and ionic conductivity. The device achieved an initial capacity of 418 mAh g^{-1} at 5 A g^{-1}, with a Coulombic efficiency of 99.4% and 70% capacity retention after 2500 cycles.

As illustrated in Figure 8, the FVO: MXene (2:1) electrode exhibits improved electrochemical performance against various test parameters. Figure 8a shows the cyclic voltammetry (CV) profiles over five cycles at a scan rate of 0.1 mV s^{-1}, showing stable and sharp redox peaks for the Fe and V species. The charge–discharge behavior is presented in Figure 8b,c. First, the GCD curves at 0.1 A g^{-1} for five cycles show good reversibility. The comparison of the voltage profiles at different current densities is shown, indicating stable capacity retention, even at higher rates. As shown in Figure 8d, the Nyquist plots and the corresponding equivalent circuit model suggest that the FVO: MXene (2:1) electrode has the lowest charge-transfer resistance among the tested configurations, attributed to the highly conductive MXene network. Figure 8e,f present the specific capacity versus the cycle number at various rates and under prolonged cycling at 100 mA g^{-1}, where the hybrid electrode outperforms both pristine FVO and MXene loadings, justifying the optimal ratio. Finally, Figure 8g illustrates the long-term cycling stability at 5 A g^{-1} in which the device has a capacity of approximately 418 mAh g^{-1}, with 99.4% Coulombic efficiency and around 70% capacity retention after 2500 cycles, thereby confirming the synergistic advantage of the use of redox-active metal oxides with conductive MXene nanosheets in achieving high-rate, long-term lithium-ion storage. This architecture was also adapted for

sodium-ion batteries using $NaClO_4$ in EC/DMC. Although it had a lower initial capacity of 129 mAh g^{-1}, the cell demonstrated excellent retention (81%) after 5000 cycles and maintained a Coulombic efficiency of 99.52%, indicating excellent structural stability, even when seeking to accommodate larger Na^+ ions [158].

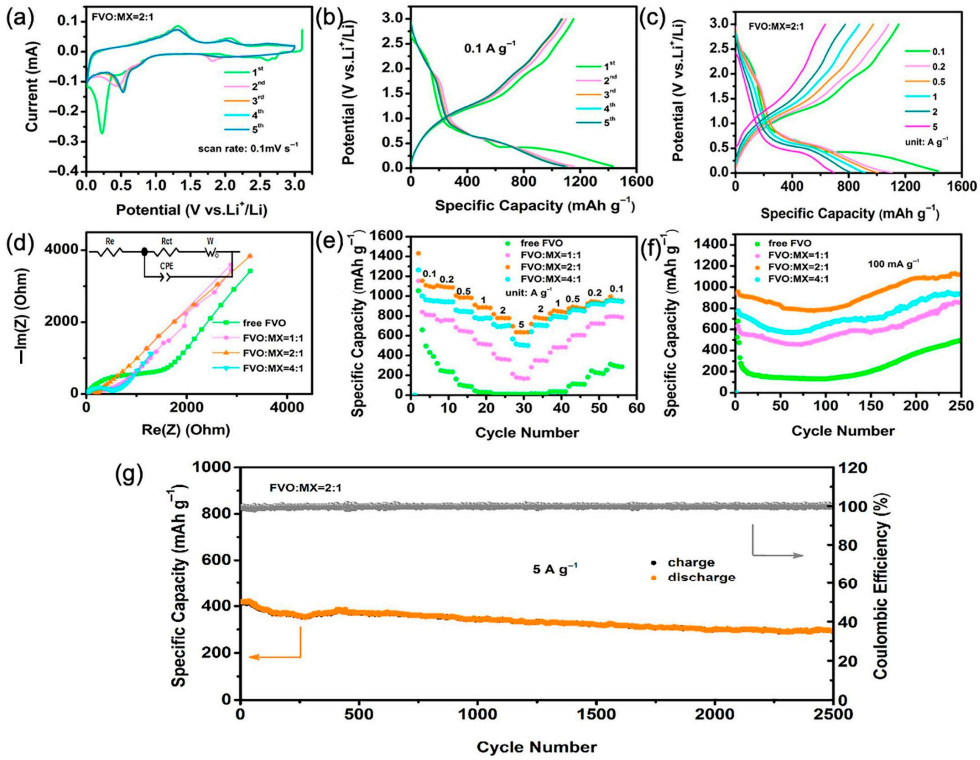


Figure 8. Electrochemical performance of $FeVO_4$/MXene (FVO: MX) hybrid electrodes in lithium-ion batteries. (**a**) CV curves. (**b**,**c**) GCD curves. (**d**) Nyquist plot. (**e**,**f**) Specific capacity over cycling at various rates. (**g**) Long-term cycling. Reprinted from Ref. [158]. Copyright 2022, with permission from Elsevier.

Another innovative design is the g-C_3N_4/$TiVCT_x$-30//$LiFePO_4$ composite, where $TiVCT_x$ is combined with graphitic carbon nitride (g-C_3N_4), a porous semiconductor with structural and catalytic properties. This combination provides additional ion transport channels, facilitating electrolyte/electrode interactions. The system uses $LiPF_6$ in EC/DEC (ethylene carbonate/diethyl carbonate) with a wide electrochemical stability window. The cell demonstrated 558.3 mAh g^{-1} at 1 A g^{-1}, retained 76.17% capacity after 1000 cycles, and exhibited 97.9% Coulombic efficiency, confirming the multifunctional role of MXene-based composites in Li-ion battery electrodes [167]. For zinc-based systems, the S-$Ti_3C_2T_x$/PANI//Zn configuration integrates $Ti_3C_2T_x$ sheets functionalized with sulfonic groups with polyaniline (PANI), a conductive polymer with high pseudocapacitive behavior. This design offers enhanced conductivity and electrochemical stability. Under 2 M $ZnSO_4$ electrolyte, the cell achieved 160 mAh g^{-1} at 15 A g^{-1}, with ~64% capacity retention over 5000 cycles and approaching 100% Coulombic efficiency. This configuration demonstrates long-term stability and high-rate capability for zinc-based energy storage [124].

The MXene/MoS_2@C//NVP system combines $Ti_3C_2T_x$ decorated with molybdenum disulfide (MoS_2) and amorphous carbon as the positive electrode, paired with a sodium vanadium phosphate (NVP) negative electrode. Operated with $NaPF_6$ in DEGDME (diethylene glycol dimethyl ether), a compatible sodium-ion electrolyte, the cell reached 230 mAh g^{-1} at 1 A g^{-1}, with 82.2% retention after 100 cycles and 97.8% Coulombic efficiency at 0.1 A g^{-1} [168]. The resulting structure maximizes conductivity and enhances ion

diffusion by using $NaCF_3SO_3$ in diglyme as the electrolyte; the cell delivered 368 mAh g^{-1} at 10 A g^{-1}, with 87.5% retention after 3000 cycles and ~100% Coulombic efficiency, making it ideal for high-power, long-life sodium storage systems [169].

Two systems are worth discussion in lithium–sulfur configurations: the first is the the 3D COF/MXene/S composite, which employs covalent organic frameworks (COFs) with MXenes hosting sulfur. Using LiTFSI in DOL/DME with 1% $LiNO_3$ as an electrolyte, the system maintained 379 mAh g^{-1} after 300 cycles with 73% retention and 95% Coulombic efficiency [170]. The second system uses $Ti_3C_2T_x$–TiO_2/ZnS as the sulfur host, operating with Li_2S_6 in DOL/DME. It achieved 1002.9 mAh g^{-1} at 0.5C, with 56% retention after 500 cycles, suggesting a high initial performance but a need for enhanced cycling stability [171].

The TNO@MXene architecture consists of titanium–niobium oxide microspheres, encapsulated by MXene layers, providing high conductivity and surface area. Using $LiPF_6$ in EC/DEC, it delivered 200.3 mAh g^{-1} at 20 C, retained 66% after 1400 cycles, and maintained 94.4% Coulombic efficiency [172]. In sodium-ion systems, MXene@SnS_2—prepared via HF etching and functionalized with a tin disulfide—served as an anode in a $NaPF_6$/DME electrolyte, delivering 288.1 mAh g^{-1} after 100 cycles with 86.1% capacity retention and 82.9% Coulombic efficiency [173]. Lastly, the MXene@Ni_2P-1/S system incorporates nickel phosphide onto MXene sheets, serving as a catalytic sulfur host. Li2S6 in DOL/DME achieved ~690 mAh g^{-1} initial capacity, 72.8% retention after 300 cycles, and 99.8% Coulombic efficiency, demonstrating strong shuttle suppression and catalytic enhancement [174]. Table 2 summarizes recent MXene-based battery systems, including lithium-ion, sodium-ion, and zinc-ion configurations and their electrochemical performance metrics.

3.2. MXenes in Triboelectric Nanogenerators (TENGs)

Despite the prevailing interest in MXene-related topics relating to electrochemical energy storage, increasing interest has been observed regarding its application in triboelectric nanogenerators (TENGs). Among them, $Ti_3C_2T_x$ MXene has significantly improved triboelectric output as an active layer or additive. For example, sodium alginate-based composites containing Ti_3CN exhibited a notably higher output voltage of approximately 640 V, compared to the values of 290 V for Ti_3CN and 430 V obtained for alginate-only devices. These composites also delivered a current output of 12 μA and a peak average power density (Pav) of 0.28 W·m^{-2} at a load of 500 MΩ, with instantaneous power density reaching 6.8 W·m^{-2} at 100 MΩ. These values surpass or are comparable to those of other MXene–biopolymer TENGs reported in the literature, such as Ti_3C_2 in alginate/Ecoflex (0.05 W·m^{-2}, 1.0 μA, 200 V), cellulose nanofiber (0.5 W·m^{-2}, 5.5 μA, 300 V), carboxymethyl cellulose (0.4 W·m^{-2}, 0.8 μA, 120 V), and poly(lactic acid) (0.5 W·m^{-2}, 22 μA, 100 V) [27]. This superior performance is attributed to the higher density of surface terminations in Ti_3CN and stronger interfacial dipole interactions that enhance surface charge trapping and electron transfer. Consequently, surface functionalization affects the triboelectric behavior of MXene-based devices since, depending on their surface terminations, MXenes can act as either tribopositive or tribonegative materials. Oxygen-containing groups (-O) generally act as electron donors, whereas fluorine terminations (-F) function as electron-withdrawing groups, allowing the fine-tuning of triboelectric polarity. This dual behavior underscores the potential of exploring the broad compositional diversity of MXenes to design highly asymmetric and synergistic triboelectric pairs for advanced TENG applications. Additionally, their lamellar structure serves as an ideal scaffold for the growth of functional nanostructures, contributing to enhanced electrical conductivity, charge storage capacity, and structural stability [175].

Table 2. Electrochemical performance of MXene-based battery systems.

Structure	Device	Electrolyte	Current Rate	Initial Capacity	Cycles	Final Capacity	Coulombic Efficiency	Ref.
$Ti_3C_2T_x$//$FeVO_4$ (2:1)	Li-ion Battery	$LiPF_6$ in EC/DMC	5 $A{\cdot}g^{-1}$	418 $mAh{\cdot}g^{-1}$	2500	~70%	99.4%	[158]
$Ti_3C_2T_x$//$FeVO_4$	Na-ion Battery	$NaClO_4$ in EC/DMC	5 $A{\cdot}g^{-1}$	129 $mAh{\cdot}g^{-1}$	5000	~81%	99.52%	[158]
g-C_3N_4/$TiVCT_x$-30//$LiFePO_4$	Li-ion Battery	$LiPF_6$ in EC/DEC	1 $A{\cdot}g^{-1}$	558.3 $mAh{\cdot}g^{-1}$	1000	76.17%	97.9% after 50 cycles	[167]
S-$Ti_3C_2T_x$/PANI//Zn	Zn-ion Battery	2 M $ZnSO_4$	15 $A{\cdot}g^{-1}$	160 $mAh{\cdot}g^{-1}$	5000	~64%	~100%	[124]
MXene/MoS_2@C//NVP	Na-ion Battery	$NaPF_6$ in DEGDME	1 $A{\cdot}g^{-1}$	230 $mAh{\cdot}g^{-1}$	100	82.2%	97.8% at 0.1 $A{\cdot}g^{-1}$	[168]
$FeSe_2$ nanorods-MXene	Na-ion Battery	$NaCF_3SO_3$ in diglyme	10 $A{\cdot}g^{-1}$	368 $mAh{\cdot}g^{-1}$	3000	~87.5%	~100%	[169]
3D COF/MXene/S	Li–S Battery	LiTFSI in DOL/DME + 1% $LiNO_3$	0.5 $A{\cdot}g^{-1}$	-	300	73% 379 $mAh{\cdot}g^{-1}$	95%	[170]
$Ti_3C_2T_x$-TiO_2/ZnS	Li–S Battery	Li_2S_6 in DOL/DME	0.5 C	1002.9 $mAh{\cdot}g^{-1}$	500	~56%	-	[171]
TNO@MXene	Li-ion Battery	$LiPF_6$ in EC/DEC	20 C	200.3 $mAh{\cdot}g^{-1}$	1400	~66%	94.4%.	[172]
MXene@SnS_2	Na-ion Battery	$NaPF_6$ in DME	1	288.1 $mAh{\cdot}g^{-1}$	100	86.1%	82.9%	[173]
MXene@Ni_2P-1/S	Li–S Battery	Li_2S_6 em DOL/DME	1 C	~690 $mAh{\cdot}g^{-1}$	300	72.8%	99.8%	[174]

Incorporating MXene into TENGs involves their intrinsic electrical conductivity, layered structure, and large specific surface area, making them ideal as electrodes or functional additives in triboelectric layers. TENGs operate based on the triboelectric effect and electrostatic induction, generating charge upon periodic contact and separation between materials with different electron affinities. Underutilized as electrode materials in TENGs, MXenes significantly enhance charge collection and transport efficiency—their lamellar morphology guarantees contact with triboactive polymers such as PDMS, PVA, or alginate. Furthermore, surface terminations such as -OH and -F groups facilitate compatibility with hydrogels and polymer composites, inducing interface adhesion. MXenes have also been explored as functional materials to control the triboelectric polarity of active surfaces. For instance, when incorporated within PDMS or Kapton matrices, MXenes regulate the electron-donating or electron-accepting nature of the surface, enabling its position regulation on the triboelectric series. This adjustment enhances open-circuit voltage and short-circuit current while supporting mechanical durability and cycling stability. Additionally, MXenes decorated with metals or metal oxides, such as MXene@CuO or NH_2-MXene/TiO_2, have demonstrated bifunctional behavior in TENGs, enabling their simultaneous use as energy harvesters and chemical sensors. This multifunctionality broadens their application in self-powered cathodic protection, gas sensing, and environmental monitoring. The incorporation of MXenes into TENGs significantly improves electrical output and device durability, making them well-suited for wearable energy harvesting systems.

The influence of MXene chemical composition on triboelectric characteristics and TENG device performance was demonstrated in studies by Wicklein et al. [27], investigating sodium alginate composites with Ti_3C_2 and Ti_3CN. They showed that Ti_3C, with its higher surface functional group density, supports stronger hydrogen bonding with alginate chains, improving surface charge density and electrostatic coupling. Therefore, Ti_3CN-based composites exhibited significantly higher electrical output than their Ti_3C_2-based counterparts. Ti_3C_2 and Ti_3CN MXene nanosheets were incorporated into alginate matrices using solution blending and drop casting on carbon paper substrates to obtain hierarchical lamellar structured composite films, as illustrated in Figure 9a. SEM images confirm the accordion-like morphology of the pristine MXenes and the uniform topography of the resulting composite surface. Using sodium alginate as a biopolymer makes it easy to create a film and introduce -COOH and -OH functional groups that can form hydrogen bonds with MXene surfaces. Figure 9b details the multilayer architecture of the TENG device, including the MXene–alginate-coated carbon paper and the Al/FEP layers as counter electrodes. A schematic illustrates the interfacial hydrogen bonding between the oxygen-containing groups of alginate and the surface-terminated functionalities (-F, -O, -OH) of Ti_3CN, which are present in greater abundance than Ti_3C_2, and enhanced surface chemistry results in stronger dipole interactions and higher surface charge density. Therefore, the output voltage profiles confirm this effect: the Ti_3CN-alginate TENG produces much greater triboelectric output than its Ti_3C_2-based counterpart, enhancing the essential role of MXene surface chemistry in optimizing triboelectric performance.

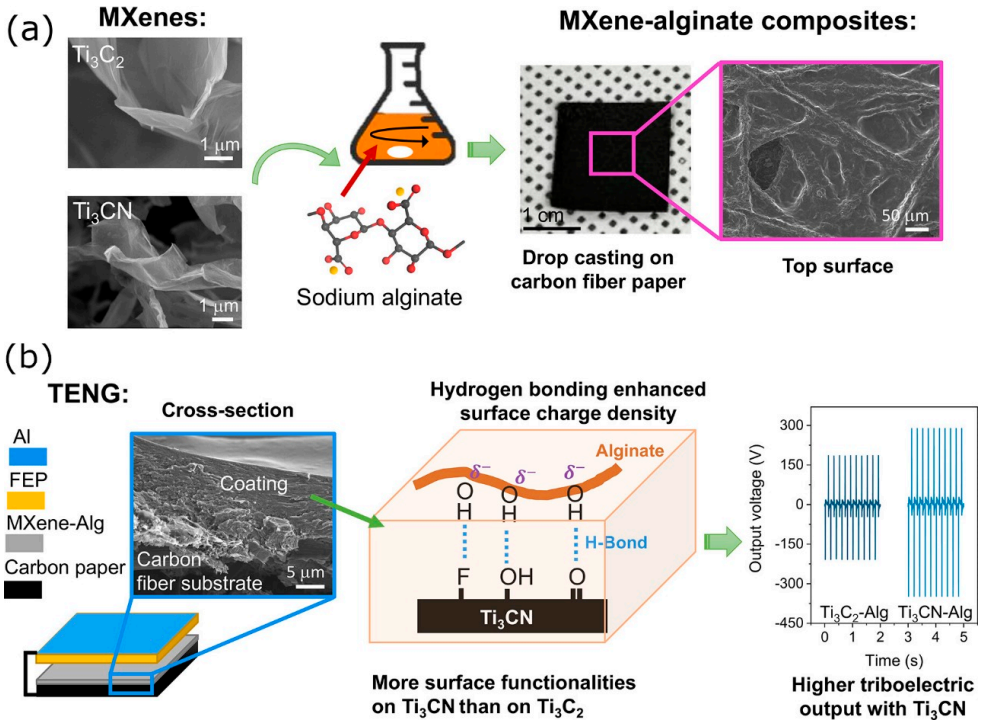


Figure 9. (**a**) Schematic synthesis of MXene-alginate composites, with corresponding SEM images. Atom color code in alginate structure: C (gray), O (red), Na (light yellow). (**b**) TENG cross-section, hydrogen bonding mechanism, and enhanced triboelectric voltage in MXene-alginate composites. Adapted from Ref. [27]. Published under a Creative Commons CC-BY 4.0 license.

3.2.1. Integration of MXene in TENGs for Self-Powered Devices

Recent examples of MXene-based triboelectric nanogenerators, including examples of structure, performance output, and triboelectric roles, are compiled in Table 3. Wei and Sun (2025) fabricated a conductive double-network hydrogel (SA/MXene/PAAm) that, when used in a wearable TENG, generated up to 492 V, 75.4 μA, and 2.54 mW (at 3 MΩ load) [176]. Wang et al. (2021) utilized MXene@CuO composites with outputting performances of 810 V and 10.84 W m^{-2} and also enabled selective ammonia gas detection [177]. In another work, Wang et al. (2025) fabricated an NH_2-MXene/TiO_2@alginate multilayered TENG, with an output of 357.6 V and 3.9 mW power, which can be used for self-powered cathodic protection [178]. Another high-performance architecture, BW-TENG, employed B-MXene, Kapton, and PVA to attain 5.66 W·m^{-2} power density and 25 μA current output with multimodal functionality [179]. Furthermore, Wicklein et al. (2024) showed that the specific MXene composition significantly influences triboelectric behavior, demonstrating the MXene phases' tunability for particular TENG applications [27].

3.2.2. Applications in Wearable Sensors and Sustainable Energy Systems

MXene–polymer composites, such as MXene@PDMS, have been widely explored to develop flexible and stretchable TENGs. For instance, ZIF-8/MXene@PDMS-based devices have achieved voltages of 162 V, demonstrating efficacy in harvesting energy from raindrops and human motion [175]. A PAM/CNF/MXene hydrogel-based TENG produced up to 67.5 V under 100% strain for wearable sensors, underscoring its potential in human–machine interface applications [154]. Similarly, chitosan aerogels containing 2 wt% MXene have been proposed as lightweight, functional solutions for energy harvesting and electromagnetic interference shielding [180].

Table 3. MXene-based triboelectric nanogenerators (TENGs).

Structure/Composition	Open-Circuit Voltage (V)	Short-Circuit Current (μA)	Power Output	Ref.
SA/MXene/PAAm Hydrogel TENG	491.98	75.41	2.54 mW with 3 MΩ.	[176]
TA@CNC/MXene Hydrogel (N-TENG)	68.04	1.02	69.97 $mW \cdot m^{-2}$	[152]
Ti3CN–Alginate TENG	670	15	0.28 $W \cdot m^{-2}$	[27]
MXene/CuO composite	810	34	10.84 $W \cdot m^{-2}$	[177]
PAM/CNF/MXene Hydrogel	67.5 (under 100% strain)	0.13		[154]
Chitosan aerogel + 2 wt% MXene	110	1.9		[180]
BW-TENG (Al/B-MX/Kapton/PVA)	120	25	5.66 $W \cdot m^{-2}$	[179]
NMTS-TENG (NH2-MXene/TiO2)	357.6	55.1	3.9 mW	[178]
ZIF-8/MXene@PDMS	162	6.1		[175]

3.3. MXenes in Sensors and Flexible Electronics

MXenes are a rapidly emerging family of two-dimensional materials that have demonstrated outstanding potential in developing hybrid sensors and flexible electronics due to their unique combination of high electrical conductivity, mechanical flexibility, and surface functionalization. Table 4 summarizes the electrochemical characteristics and functional applications of MXene-based sensor composites, including gas sensitivity, pressure response, linearity, and cycling performance. This compilation highlights the wide range of MXene integrations and their effectiveness in biomedical, chemical, and environmental detection, reinforcing their suitability for flexible and multifunctional sensing platforms. The data cover applications such as gas sensors, triboelectric nanogenerators (TENGs), and strain sensors, illustrating the multidimensional sensing capabilities provided by MXene's lamellar structure and surface chemistry.

3.3.1. Development of Hybrid Sensors for Biomedical, Gas, and Pressure Detection

Integrating MXenes into hybrid sensors has yielded impressive results in various areas. Due to their biocompatibility, sensitivity, and mechanical compliance, MXene-based composites have found applications in the biomedical field for physiological monitoring, such as heart rate, muscle activity, and motion. Alex et al. developed flexible electrodes derived from $Ti_3C_2T_x$ MXene with excellent electrochemical performance and stability for wearable bioelectronics [122]. In gas detection tests, MXene/metal-organic framework (MOF)/CuO composites are utilized in TENG-powered sensors for ammonia detection, with rapid and selective responses, thus verifying MXene's role in high-sensitivity chemical sensing [177]. MXene composites with gold nanoparticles display improved electrochemical activity in terms pesticide and biomolecule sensing due to their synergistic catalytic and conductive properties [145]. Surface functionalization with polymeric coats has also improved gas-sensor selectivity and environmental stability. According to Figure 10, Choi et al. demonstrated the impact of fluorinated polymer functionalization on the gas-sensing performance of the p(PFDMA)-coated $Ti_3C_2T_x$ MXenes. In Figure 10a, time-resolved gas response curves are shown for both pristine and p(PFDMA)-coated MXenes when exposed to five volatile organic compounds (VOCs): hexane, toluene, ethanol,

propanal, and acetone. The polymer-functionalized sensor exhibits narrower response peaks and faster recovery, particularly for nonpolar analytes, indicating enhanced VOC transport and selectivity. Figure 10b quantifies the gas response to all analytes, confirming that the p(PFDMA)/$Ti_3C_2T_x$ composite has significantly increased sensitivity to hexane and toluene compared to unmodified MXene while suppressing responses to polar solvents like ethanol and acetone, highlighting the role of the polymer layer in modulating chemical affinity and diffusion at the sensor interface. Figure 10c also examines the sensor response to acetone at elevated concentrations (1–5 ppm), which shows a linear relationship with both pristine and functionalized MXenes but has a reduced slope in the polymer-coated case, indicating reduced acetone uptake due to the fluorinated layer. Figure 10d shows the long-term sensing performance for 5 ppm hexane. The p(PFDMA)/$Ti_3C_2T_x$ sensor shows faster rise and fall times, which can be attributed to greater diffusion efficiency across the polymer matrix and lower adsorption at the surface. The outcome again confirms that polymer functionalization enables fast, reversible sensing behavior. Finally, Figure 10e shows a comparative schematic mechanism. Pristine MXene relies on direct gas adsorption on the surface, where saturation is a threat, and responses will be slow. On the other hand, the p(PFDMA) layer adds free volume that can facilitate gas diffusion, allowing controlled interaction with the MXene surface and promoting selective, faster, and more stable gas detection [95].

MXene/MWCNT composites have been engineered in pressure and strain sensors as self-healing, low-percolation-threshold materials with high sensitivity. Experimental studies demonstrated their effectiveness in real-time pressure detection and structural health monitoring applications [125].

3.3.2. Emerging Applications in Wearable and Flexible Electronics

MXenes have emerged as outstanding candidates for use in next-generation wearable and flexible electronics, with the fabrication of ultrathin, flexible, and multifunctional films that can serve as active or passive devices for electronic skins, smart textiles, on-skin biosensors, and human–machine interfaces. A key trend is the real-time monitoring of human movement, where MXene-based pressure and strain sensors are laminated on clothing or embedded into clothes. The sensors can track gait, joint movement, breathing, and gestures. For example, Wei and Sun (2025) prepared a double-network hydrogel based on sodium alginate (SA), MXene, and polyacrylamide (PAAm). This was also a triboelectric nanogenerator (TENG) and generated 492 V and 75.4 μA in mechanical movement [176]. A similar experiment involved a hydrogel sensor combining PAM, CNF, and $Ti_3C_2T_x$ MXene. It achieved 67.5 V at 100% strain and performed well in terms of sensing finger bending and knee flexion [154]. These sensors are sensitive, stretchable, and appropriate for soft robotics, physical rehabilitation, and digital health monitoring. Self-healing MXene/MWCNT elastomer sensors with extremely low percolation thresholds and high-pressure sensitivity have been developed. Fu et al. demonstrated the use of atomistic simulations to confirm their dynamic network formation and potential for self-repair in wearable applications [125].

Table 4. MXene-based composite sensors.

Sensing Material	Sensor Type	Target Analyte	Mechanism	Performance	Application	Ref.
MXene/MWCNT/ITT Elastomer	Strain Sensor (Self-healing)	Mechanical deformation	Piezoresistive (dynamic bonding)	Self-healing efficiency up to 100%@80 °C; recovery of 74.3% mechanical and 94.8% electrical properties; GF = 1.0; low threshold (3.5 wt%) for conduction	Wearable strain sensors, e-skin, robotics	[125]
$Ti_3C_2T_x$/PDMS/Glycerol Composite	Biomedical (ECG, EMG)	Biopotentials (skin)	Electrochemical	Bulk impedance: 280–111 Ω; conductivity: 0.462–1.533 mS/cm; charge storage: 0.665–1.99 mC/cm^2; elongation: 139–144%;	Wearable skin biosignal sensing (ECG, EMG), long-term electrode applications	[122]
AChE-Chit/MXene/Au NPs/MnO_2/Mn_3O_4/GCE	Electrochemical Sensor	Pesticides (methamidophos)	Enzymatic inhibition electrochemical	LOD: 1.34 × 10^{-13} M; range: 10^{-12}–10^{-6} M; recovery 95.2–101.3%	Electrochemical pesticide detection	[145]
$Ti_3C_2T_x$/CuO (MOF-derived)	Gas Sensor (Ammonia)	Ammonia (NH_3)	Triboelectric	Response ~24.8@100 ppm; TENG: 810 V, 34 μA, 10.84 W/m^2;	Wearable flexible format Self-powered ammonia detection	[177]
$Ti_3C_2T_x$ + p(PFDMA)	Stability-Enhanced Gas	VOC gases	Surface modification (polymer coating)	SNR retained under 50 °C/100% RH for 3 weeks; SNR 8.3× higher than uncoated MXene;	Enhanced environmental stability and sensor durability	[95]
MXene/SA Double-Network Hydrogel	TENG (Triboelectric Generator)	Mechanical motion (foot/joint)	Triboelectric	VOC: 491.98 V; ISC: 75.41 μA; QSC: 83.93 nC; power: 2.54 mW@3 MΩ; +84% output vs. conventional	Sports monitoring, motion sensing, self-powered wearable electronics	[176]
PAM/CNF/MXene Hydrogel	Strain Sensor + TENG	Strain (1–550%)	Triboelectric + piezoresistive	Strain: 1–550%; GF: 6.73; response time: 100 ms; recovery: 110 ms; Voc: 67.5 V @100% strain; 550% elongation, 0.31 MPa	Motion sensing, writing recognition, energy harvesting, info transmission	[154]
3D-Printed Chitosan/MXene Aerogel	TENG + EMI Shielding	Mechanical motion + EM signals	Triboelectric + electromagnetic attenuation	TENG output: 22 V (0 wt%), 110 V (2 wt%), current: 1.9 μA; EMI shielding: up to 28 dB (81% absorption);	Energy harvesting, EMI shielding, thermal insulation	[180]
PEDOT:PSS/MXene/Ag Grid	FTS (Flexible Transparent Supercapacitor)	Human activity	Capacitive + sensing (Electrochemical)	Transparency: 60–71%; areal capacitance: 3.7–12 mF/cm^2; optical transmittance ≈ 89%	Energy storage + sensing + transparency for smart wearable devices	[19]
Tannin/CNC/MXene (TMCN) Hydrogel	Strain Sensor + TENG	Motion, biosignals, handwriting	Ionic conduction + triboelectric	Strain: up to 3718%; toughness: 12.14 MJ/m^3; gauge factor: 14.5; Voc: 68.04 V; Isc: 1.02 μA; Qsc: 22.66 nC; Power: 69.97 mW/m^2;	Motion sensing, self-powered messaging, healthcare (Morse code)	[152]

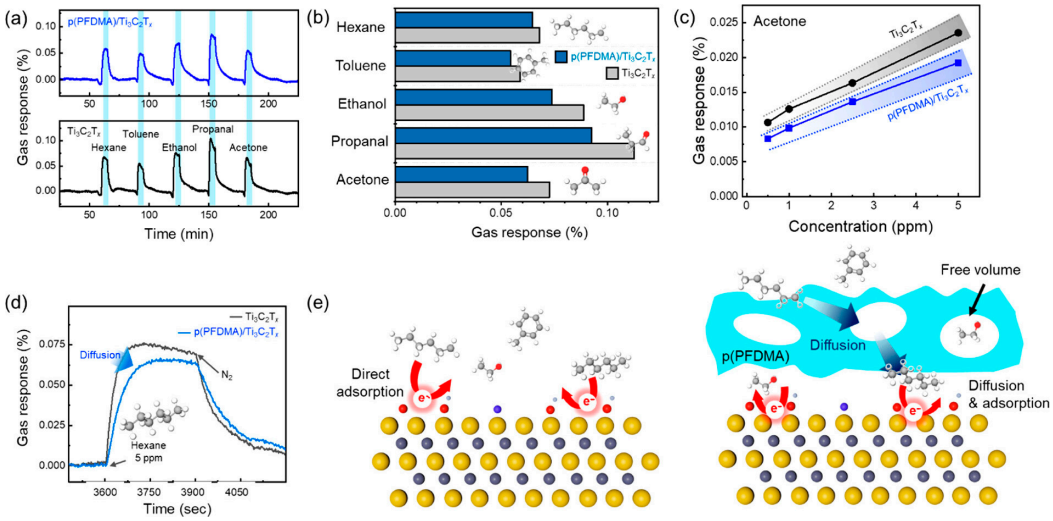


Figure 10. Gas-sensing performance and mechanism of $Ti_3C_2T_x$ and p(PFDMA)/$Ti_3C_2T_x$ MXene composites. (**a**) Dynamic gas response curves. (**b**) Bar graph showing gas response. (**c**) Sensor response. (**d**) Long-term detection of 5 ppm hexane. (**e**) Schematic illustration comparing direct adsorption of pristine MXene with diffusion-mediated adsorption in p(PFDMA)/$Ti_3C_2T_x$. Atom color code in (**e**): Ti (yellow), C (gray), O (red), F (blue), H (white). Adapted with permission from Ref. [95]. Copyright 2023 American Chemical Society.

MXenes have also been comprehensively investigated for use in transparent and flexible electronics. Cheng et al. constructed a hybrid capacitive sensor using MXene, PEDOT:PSS, and Ag grids. The sensor displayed good areal capacitance and good signal response to bending stress [19]. Such systems support integration into foldable displays, e-skin technologies, and touch-enabled wearables. In multifunctional hydrogel sensors, Wang et al. fabricated a strain sensor based on MXene and tannin-derived nanoparticles that are conductive even at subzero temperatures and in wet conditions. Its tensile cycling and high-strain-rate performance confirm its potential for use in harsh environments [152]. For electromagnetic interference (EMI) shielding and multifunctional integration, 3D-printed MXene/chitosan aerogels showed effective EMI shielding, mechanical responsiveness, and thermal regulation, making them suitable for industrial applications and protective clothing [180].

MXenes are also being integrated into self-powered gas-sensing platforms. Zhang et al. fabricated a multifunctional TENG-powered ammonia sensor based on MXene/MOF-derived CuO, with the quick and selective sensing of NH_3 for organ-like monitoring devices [177]. Wang et al. also fabricated a TENG with NH_2-MXene/TiO_2@SA films for autonomous cathodic protection, reflecting new directions for energy-autonomous corrosion monitoring [178]. This in-depth analysis in the field of chemical sensing was followed by an increase in $Ti_3C_2T_x$ MXene selectivity to volatile organic compounds using perfluorinated polymer coating via iCVD. It facilitated the detection of VOCs, even at high humidity values, enabling the long-term use of wearable gas monitors [95]. Such developments attest to the versatility of MXene in countless wearable technology applications.

4. Challenges and Future Perspectives

The intrinsic properties of MXenes position them as leading candidates for energy storage, sensing, and flexible electronics applications. However, environmental stability, eco-friendly synthesis, and structural innovation challenges still inhibit their widespread usage in industrial-scale technologies. One major drawback is the long-term ecological stability of MXenes, particularly $Ti_3C_2T_x$ because it oxidizes in wet air due to the hydrophilicity of the surface. Although it has minor structural deterioration, adding moisture

plays a significant role in electrical conductivity. Conductivity has also been partially restored through vacuum annealing in experiments, and up to nine years' long-term storage is demonstrated not to damage the lamellar structure irreparably [93]. Other techniques, such as hydrophobic protection layer deposition, dry or inert atmospheres for storage, and surface organic or inorganic functional group modification, have also prevented degradation [95]. Additional chemical stability is formed, and other technologies, including polymer encapsulation and heteroatom doping, ensure electrochemical performance [181].

Synthesis, scalability, and environmental sustainability are key barriers to commercialization. Conventional MXene synthesis relies on harmful etching reagents such as HF or fluoride-based solutions, which limit industrial use. Recent techniques such as molten salt exfoliation and electrochemical etching have been developed to address this limitation, with enhanced control over surface chemistry while avoiding corrosive reagents [182]. These routes support safer, more reproducible production, and research into automation and continuous-flow synthesis will improve yield and reduce waste [99]. The new architecture is also central to advancing MXene technology in materials engineering. Three-dimensional porous networks of $Ti_3C_2T_x$, prepared by surfactant-assisted self-assembly at oil/water interfaces, enhance the surface area and accessibility of ions. These architectures are appropriate for stretchable sensors and high-performance supercapacitors, with better mechanical stability and transport channels [183].

Artificial intelligence (AI) integration is accelerating the discovery and optimization of MXene-based materials. Machine learning (ML) algorithms have been employed to predict electrochemical, piezoelectric, and mechanical properties across broad compositional spaces. For example, a recent study screened 680 different MXene compositions using an ML pipeline trained on DFT-calculated descriptors, successfully identifying new candidates with enhanced pseudocapacitive performance [184]. In another work, ML-assisted modeling using regression algorithms and active learning identified nine functionalized monolayer MXenes with out-of-plane piezoelectric strain coefficients exceeding 2 pm/V. Overall, 22 different MXenes exhibited strong and stable piezoelectric responses, confirming their promise for nanoelectromechanical systems (NEMS) [185]. Furthermore, an autonomous system integrating robotic synthesis and ML-optimized 264 formulations of MXene–CNF–gelatin aerogels was explored using a machine learning-guided autonomous platform combining Gaussian process regression with robotic synthesis. The system simultaneously optimized compressive modulus and electrical resistance, identifying candidate formulations with low stiffness and enhanced conductivity [186]. These advancements highlight how AI has transitioned from a conceptual tool to a practical framework for guiding MXene material design. The integration of active learning, generative design, and reinforcement learning approaches is expected to drive further innovation in scalable, high-performance MXene-based systems.

Author Contributions: Conceptualization, J.A.A.F. and H.P.d.O.; methodology, J.A.A.F. and H.P.d.O.; data curation, J.A.A.F. and H.P.d.O.; writing—original draft preparation, J.A.A.F. and H.P.d.O.; writing—review and editing, J.A.A.F. and H.P.d.O.; visualization, J.A.A.F. and H.P.d.O.; supervision, H.P.d.O. All authors have read and agreed to the published version of the manuscript.

Funding: This research was supported by Brazilian funding agencies Coordenação de Aperfeiçoamento de Pessoal de Nível Superior—Brasil (CAPES) Finance Code 001, FINEP, FACEPE, and CNPq (Grant No. 303997/2021-4).

Data Availability Statement: All data are contained within the article.

Acknowledgments: Brazilian funding agencies Coordenação de Aperfeiçoamento de Pessoal de Nível Superior—Brasil (CAPES) Finance Code 001, FINEP, FACEPE, and CNPq (Grant No. 303997/2021-4).

Conflicts of Interest: The authors declare no conflicts of interest.

Abbreviations

The following abbreviations are used in this manuscript:

AC	activated carbon
AI	artificial intelligence
Bi	bismuth
CDP	cyclodextrin polymer
CNC	cellulose nanocrystals
CNT	carbon nanotube
Co_9S_8	cobalt sulfide
COF	covalent organic framework
CoO	cobalt(II) oxide
CuO	copper(II) oxide
CV	cyclic voltammetry
DEC	diethyl carbonate
DEGDME	diethylene glycol dimethyl ether
DMC	dimethyl carbonate
DMSO	dimethyl sulfoxide
DOL/DME	1,3-dioxolane/dimethoxyethane
EC	ethylene carbonate
EDLC	electrical double-layer capacitance
EDX	energy-dispersive X-ray spectroscopy
EMI	electromagnetic interference
EMIMTFSI	1-ethyl-3-methylimidazolium bis(trifluoromethanesulfonyl)imide
$FeVO_4$	iron vanadate
FVO	$FeVO_4$ (iron vanadate)
g-C_3N_4	graphitic Carbon Nitride
GCD	galvanostatic charge–discharge
GeOx	germanium oxide
H_2SO_4	sulfuric acid
HRTEM	high-resolution transmission electron microscopy
$K_4[Fe(CN)_6]$	potassium ferrocyanide
KOH	potassium hydroxide
$LiFePO_4$	lithium iron phosphate
$LiPF_6$	lithium hexafluorophosphate
LiTFSI	lithium bis(trifluoromethanesulfonyl)imide
ML	machine learning
MnO_2	manganese dioxide
$Mo_2TiC_2T_X$	double transition metal MXene composed of molybdenum and titanium atoms
$Mo_4VC_4T_x$	molybdenum vanadium carbide MXene
MOF	metal-organic framework
MoS_2	molybdenum disulfide
MWCNT	multi-walled carbon nanotube
$NaClO_4$	sodium perchlorate
$NaPF_6$	sodium hexafluorophosphate
Nb_2C	niobium carbide
NH_2	amine group
NH_3	ammonia
NH_4Cl	ammonium chloride

NiCoP	nickel cobalt phosphide
Ni-MOF	nickel-based metal-organic framework
NPO	nickel phosphate
NVP	sodium vanadium phosphate
p(PFDMA)	poly(perfluorodecyl methacrylate)
PAAm	polyacrylamide
PANI	polyaniline
Pav	average power density
PEDOT:PSS	poly(3,4-ethylenedioxythiophene):poly(styrenesulfonate)
PLA	polylactic acid
p-MC	3D interconnected porous MXene/carbon dot film
PVA	polyvinyl alcohol
PVP	Polyvinylpyrrolidone
rGO	reduced graphene oxide
S- $Ti_3C_2T_x$	sulfonation of $Ti_3C_2T_x$
SA	sodium alginate
SDS	sodium dodecyl sulfate
SEM	scanning electron microscopy
SPE	solid polymer electro
SSA	specific surface area
TEM	transmission electron microscopy
Ti_2C	titanium carbide
Ti_3C_2	titanium carbide
$Ti_3C_2T_x$	titanium carbide MXene
Ti_3CN	nitrogen-containing titanium carbide
TiO_2	titanium dioxide
TiVC	titanium-vanadium solid solution MXene
TNO	titanium–niobium oxide
UN-$Ti_3C_2T_x$	urea-assisted nitrogen-doped $Ti_3C_2T_x$
VS_2	vanadium disulfide
V_2CT_x	vanadium carbide MXene with surface terminations
$V_4C_3T_X$	vanadium carbide MXene with four vanadium and three carbon layers, functionalized with surface terminations
ZIF	zeolitic imidazolate framework
Zn	zinc
ZnS	zinc sulfide
$ZnSO_4$	zinc sulfate
βCD	beta-cyclodextrin

References

1. Aghmadi, A.; Mohammed, O.A. Energy Storage Systems: Technologies and High-Power Applications. *Batteries* **2024**, *10*, 141. [CrossRef]
2. Krichen, M.; Basheer, Y.; Qaisar, S.M.; Waqar, A. A Survey on Energy Storage: Techniques and Challenges. *Energies* **2023**, *16*, 2271. [CrossRef]
3. Ryu, H.; Yoon, H.J.; Kim, S.W. Hybrid Energy Harvesters: Toward Sustainable Energy Harvesting. *Adv. Mater.* **2019**, *31*, 1802898. [CrossRef]
4. Singh, J.; Kaur, R.; Singh, D. Energy harvesting in wireless sensor networks: A taxonomic survey. *Int. J. Energy Res.* **2021**, *45*, 118–140. [CrossRef]
5. Yan, W.; Ma, L.; Xu, J.; Guo, Y.; Hu, H.; Zhi, C.; Ho, D. Battery-Sensor Hybrid: A New Gas Sensing Paradigm with Complete Energy Self-Sufficiency. *ACS Appl. Mater. Interfaces* **2021**, *13*, 46507–46517. [CrossRef] [PubMed]

6. Cui, M.; Meng, X. Overview of transition metal-based composite materials for supercapacitor electrodes. *Nanoscale Adv.* **2020**, *2*, 5516–5528. [CrossRef] [PubMed]
7. Wang, K.; Wang, Z.; Liu, J.; Li, C.; Mao, F.; Wu, H.; Zhang, Q. Enhancing the Performance of a Battery-Supercapacitor Hybrid Energy Device through Narrowing the Capacitance Difference between Two Electrodes via the Utilization of 2D MOF-Nanosheet-Derived Ni@Nitrogen-Doped-Carbon Core-Shell Rings as Both Negative and P. *ACS Appl. Mater. Interfaces* **2020**, *12*, 47482–47489. [CrossRef]
8. Khuje, S.; Alshatnawi, F.; Alhendi, M.; Yu, J.; Sheng, A.; Huang, Y.; Zhuang, C.G.; Armstrong, J.; Zhou, C.; Poliks, M.; et al. High-Temperature Oxidation-Resistant Printed Copper Conductors. *Adv. Electron. Mater.* **2023**, *9*, 2200979. [CrossRef]
9. Liang, Z.; Nafis, M.S.; Rodriguez, D.; Ban, C. Surface Science and Engineering for Electrochemical Materials. *Acc. Chem. Res.* **2024**, *57*, 3102–3112. [CrossRef]
10. Mateen, A.; Khan, A.J.; Zhou, Z.; Mujear, A.; Farid, G.; Yan, W.; Li, H.; Li, J.; Bao, Z. Silicon Nanowires via Metal-Assisted Chemical Etching for Energy Storage Applications. *ChemSusChem* **2024**, *18*, e202400777. [CrossRef]
11. Pietrzak, T.K.; Wasiucionek, M.; Garbarczyk, J.E. Towards higher electric conductivity and wider phase stability range via nanostructured glass-ceramics processing. *Nanomaterials* **2021**, *11*, 1321. [CrossRef] [PubMed]
12. Humayun, M.; Bououdina, M.; Usman, M.; Khan, A.; Luo, W.; Wang, C. Designing State-of-the-Art Gas Sensors: From Fundamentals to Applications. *Chem. Rec.* **2024**, *24*, e202300350. [CrossRef] [PubMed]
13. Nunes Simonetti, E.A.; Cardoso de Oliveira, T.; Enrico do Carmo Machado, Á.; Coutinho Silva, A.A.; Silva dos Santos, A.; de Simone Cividanes, L. TiO_2 as a gas sensor: The novel carbon structures and noble metals as new elements for enhancing sensitivity—A review. *Ceram. Int.* **2021**, *47*, 17844–17876. [CrossRef]
14. Tovar-Lopez, F.J. Recent Progress in Micro- and Nanotechnology-Enabled Sensors for Biomedical and Environmental Challenges. *Sensors* **2023**, *23*, 5406. [CrossRef]
15. Costa, R.S.; Pires, A.L.; Pereira, A.M.; Pereira, C.R. Multifunctional energy harvesting and storage textile technology based on thermionic effect. *J. Power Sources* **2023**, *587*, 233712. [CrossRef]
16. Huo, D.; Yang, X.; Pan, Y.; Su, J. Gravity-Switch-Triggered Triboelectric Nanogenerator for Multi-Directional Wave Energy Harvesting. *Adv. Mater. Technol.* **2025**, *10*, 2401796. [CrossRef]
17. Kumar, R.; Kumar, A.; Shukla, P.S.; Varma, G.D.; Venkataraman, D.; Bag, M. Photorechargeable Hybrid Halide Perovskite Supercapacitors. *ACS Appl. Mater. Interfaces* **2022**, *14*, 35592–35599. [CrossRef]
18. Teixeira, J.S.; Costa, R.S.; Guedes, A.; Pereira, A.M.; Pereira, C.R. Fabrication of CNT-N@Manganese Oxide Hybrid Nanomaterials through a Versatile One-Pot Eco-Friendly Route toward Engineered Textile Supercapacitors. *ACS Appl. Eng. Mater.* **2024**, *2*, 1170–1189. [CrossRef]
19. Cheng, T.; Yang, X.; Yang, S.; Li, L.; Liu, Z.-T.; Qu, J.; Meng, C.-F.; Li, X.-C.; Zhang, Y.-Z.; Lai, W.-Y. Flexible Transparent Bifunctional Capacitive Sensors with Superior Areal Capacitance and Sensing Capability based on PEDOT:PSS/MXene/Ag Grid Hybrid Electrodes. *Adv. Funct. Mater.* **2023**, *33*, 2210997. [CrossRef]
20. Li, Y.; Shao, H.; Lin, Z.; Lu, J.; Liu, L.; Duployer, B.; Persson, P.O.Å.; Eklund, P.; Hultman, L.; Li, M.; et al. A general Lewis acidic etching route for preparing MXenes with enhanced electrochemical performance in non-aqueous electrolyte. *Nat. Mater.* **2020**, *19*, 894–899. [CrossRef]
21. Naguib, M.; Kurtoglu, M.; Presser, V.; Lu, J.; Niu, J.; Heon, M.; Hultman, L.; Gogotsi, Y.; Barsoum, M.W. Two-Dimensional Nanocrystals Produced by Exfoliation of Ti3AlC2. *Adv. Mater.* **2011**, *23*, 4248–4253. [CrossRef]
22. Naguib, M.; Mashtalir, O.; Carle, J.; Presser, V.; Lu, J.; Hultman, L.; Gogotsi, Y.; Barsoum, M.W. Two-dimensional transition metal carbides. *ACS Nano* **2012**, *6*, 1322–1331. [CrossRef]
23. Guo, Z.; Zhu, L.; Zhou, J.; Sun, Z. Microscopic origin of MXenes derived from layered MAX phases. *RSC Adv.* **2015**, *5*, 25403–25408. [CrossRef]
24. Fu, Z.H.; Zhang, Q.F.; Legut, D.; Si, C.; Germann, T.C.; Lookman, T.; Du, S.Y.; Francisco, J.S.; Zhang, R.F. Stabilization and strengthening effects of functional groups in two-dimensional titanium carbide. *Phys. Rev. B* **2016**, *94*, 104103. [CrossRef]
25. Nahirniak, S.; Ray, A.; Saruhan, B. Challenges and Future Prospects of the MXene-Based Materials for Energy Storage Applications. *Batteries* **2023**, *9*, 126. [CrossRef]
26. Luo, X.; Zhu, L.; Wang, Y.C.; Li, J.; Nie, J.; Wang, Z.L. A Flexible Multifunctional Triboelectric Nanogenerator Based on MXene/PVA Hydrogel. *Adv. Funct. Mater.* **2021**, *31*, 2104928. [CrossRef]
27. Wicklein, B.; Valurouthu, G.; Yoon, H.; Yoo, H.; Ponnan, S.; Mahato, M.; Kim, J.; Ali, S.S.; Park, J.Y.; Gogotsi, Y.; et al. Influence of MXene Composition on Triboelectricity of MXene-Alginate Nanocomposites. *ACS Appl. Mater. Interfaces* **2024**, acsami.4c03298. [CrossRef] [PubMed]
28. Ding, L.; Patel, A.; Shankar, S.; Driscoll, N.; Zhou, C.; Rex, T.S.; Vitale, F.; Gallagher, M.J. An Open-Source Mouse Chronic EEG Array System with High-Density MXene-Based Skull Surface Electrodes. *eNeuro* **2024**, *11*, ENEURO.0512-22.2023. [CrossRef]
29. Zhang, H.; Lan, D.; Wu, B.; Chen, X.; Li, X.; Li, Z.; Dai, F. Electrospun Piezoelectric Scaffold with External Mechanical Stimulation for Promoting Regeneration of Peripheral Nerve Injury. *Biomacromolecules* **2023**, *24*, 3268–3282. [CrossRef]

30. Liang, C.; Wang, H.; Lin, Z.; Zhang, C.; Liu, G.; Hu, Y. Augmented wound healing potential of photosensitive GelMA hydrogel incorporating antimicrobial peptides and MXene nanoparticles. *Front. Bioeng. Biotechnol.* **2023**, *11*, 1310349. [CrossRef]
31. Donthula, K.; Malothu, U.R.; Araga, R.; Vooradi, R.; Patnaikuni, V.S.; Reddy, M.V.; Kakunuri, M. Flexible polyaniline/MXene/CNF composite nanofibrous mats as high-performance supercapacitor electrodes. *Polym. Compos.* **2023**, *44*, 7571–7584. [CrossRef]
32. Zhang, S.; Tu, T.; Li, T.; Cai, Y.; Wang, Z.; Zhou, Y.; Wang, D.; Fang, L.; Ye, X.; Liang, B. 3D MXene/PEDOT:PSS Composite Aerogel with a Controllable Patterning Property for Highly Sensitive Wearable Physical Monitoring and Robotic Tactile Sensing. *ACS Appl. Mater. Interfaces* **2022**, *14*, 23877–23887. [CrossRef] [PubMed]
33. Zhao, G.; Sui, C.; Zhao, C.; Zhao, Y.; Cheng, G.; Li, J.; Wen, L.; Hao, W.; Sang, Y.; Zhou, Y.; et al. Supertough MXene/Sodium Alginate Composite Fiber Felts Integrated with Outstanding Electromagnetic Interference Shielding and Heating Properties. *Nano Lett.* **2024**, *24*, 8098–8106. [CrossRef] [PubMed]
34. Fatima, M.; Zahra, S.A.; Khan, S.A.; Akinwande, D.; Minár, J.; Rizwan, S. Experimental and computational analysis of mno2@v2c-mxene for enhanced energy storage. *Nanomaterials* **2021**, *11*, 1707. [CrossRef] [PubMed]
35. Myint, W.; Lolupiman, K.; Yang, C.; Woottapanit, P.; Limphirat, W.; Kidkhunthod, P.; Muzakir, M.; Karnan, M.; Zhang, X.; Qin, J. Exploring the Electrochemical Superiority of V_2O_5/TiO_2@Ti_3C_2-MXene Hybrid Nanostructures for Enhanced Lithium-Ion Battery Performance. *ACS Appl. Mater. Interfaces* **2024**, *16*, 53764–53774. [CrossRef]
36. Ruan, T.; Wang, B.; Lv, Q.; Jiang, Y.; Wang, D. Interface coupling in FeOOH/MXene heterojunction for highly reversible lithium-ion storage. *Mater. Today Energy* **2021**, *19*, 100584. [CrossRef]
37. Sun, Z.; Peng, J.; Yang, S.; Jin, R.; Liu, C.; Huang, Q. Synthesis of Low-Crystalline MnO2/MXene Composites for Capacitive Deionization with Efficient Desalination Capacity. *Metals* **2023**, *13*, 1047. [CrossRef]
38. Liu, Q.; Yang, J.; Luo, X.; Miao, Y.; Zhang, Y.; Xu, W.; Yang, L.; Liang, Y.; Weng, W.; Zhu, M. Fabrication of a fibrous MnO2@MXene/CNT electrode for high-performance flexible supercapacitor. *Ceram. Int.* **2020**, *46*, 11874–11881. [CrossRef]
39. Pathak, M.; Mane, P.; Chakraborty, B.; Rout, C.S. Facile in-situ grown spinel MnCo2O4/MWCNT and MnCo2O4/Ti3C2 MXene composites for high-performance asymmetric supercapacitor with theoretical insight. *J. Energy Storage* **2023**, *66*, 107475. [CrossRef]
40. Zhou, Z.; Panatdasirisuk, W.; Mathis, T.S.; Anasori, B.; Lu, C.; Zhang, X.; Liao, Z.; Gogotsi, Y.; Yang, S. Layer-by-layer assembly of MXene and carbon nanotubes on electrospun polymer films for flexible energy storage. *Nanoscale* **2018**, *10*, 6005–6013. [CrossRef]
41. Habib, T.; Zhao, X.; Shah, S.A.; Chen, Y.; Sun, W.; An, H.; Lutkenhaus, J.L.; Radovic, M.; Green, M.J. Oxidation stability of Ti3C2Tx MXene nanosheets in solvents and composite films. *npj 2D Mater. Appl.* **2019**, *3*, 8. [CrossRef]
42. Sunderiya, S.; Suragtkhuu, S.; Purevdorj, S.; Ochirkhuyag, T.; Bat-Erdene, M.; Myagmarsereejid, P.; Slattery, A.D.; Bati, A.S.R.; Shapter, J.G.; Odkhuu, D.; et al. Understanding the oxidation chemistry of Ti3C2T (MXene) sheets and their catalytic performances. *J. Energy Chem.* **2024**, *88*, 437–445. [CrossRef]
43. Wu, T.; Kent, P.R.C.; Gogotsi, Y.; Jiang, D. How Water Attacks MXene. *Chem. Mater.* **2022**, *34*, 4975–4982. [CrossRef]
44. Huang, S.; Mochalin, V.N. Hydrolysis of 2D Transition-Metal Carbides (MXenes) in Colloidal Solutions. *Inorg. Chem.* **2019**, *58*, 1958–1966. [CrossRef]
45. Zhang, J.; Kong, N.; Hegh, D.; Usman, K.A.S.; Guan, G.; Qin, S.; Jurewicz, I.; Yang, W.; Razal, J.M. Freezing Titanium Carbide Aqueous Dispersions for Ultra-long-term Storage. *ACS Appl. Mater. Interfaces* **2020**, *12*, 34032–34040. [CrossRef] [PubMed]
46. Fan, B.; Zhao, X.; Zhang, P.; Wei, Y.; Qiao, N.; Yang, B.; Soomro, R.A.; Zhang, R.; Xu, B. Effect of Sodium Dodecyl Sulfate on Stability of MXene Aqueous Dispersion. *Adv. Sci.* **2023**, *10*, 2300273. [CrossRef]
47. Wang, G.; Jiang, N.; Zhang, Z.; Wang, G.; Cheng, K. Free-standing 3D porous energy hydrogels enabled by ion-induced gelation strategy for High-performance supercapacitors. *Appl. Surf. Sci.* **2022**, *604*, 154636. [CrossRef]
48. Akir, S.; Lontio Fomekong, R.; Chacko, L.; Děkanovský, L.; Mazánek, V.; Sturala, J.; Koňáková, D.; Sofer, Z. Nanoengineering bismuth-modified vanadium carbide MXene for enhanced electrochemical performance in neutral electrolyte: A pathway toward high-performance supercapacitors. *J. Energy Storage* **2024**, *85*, 110962. [CrossRef]
49. Jin, Y.; Geng, J.; Wang, Y.; Zhao, Z.; Chen, Z.; Guo, Z.; Pei, L.; Ren, F.; Sun, Z.; Ren, P.-G. Flexible all-solid-state asymmetric supercapacitor based on $Ti_3C_2T_x$ MXene/graphene/carbon nanotubes. *Surfaces Interfaces* **2024**, *53*, 104999. [CrossRef]
50. Xiong, K.; Wang, P.; Yang, G.; Liu, Z.; Zhang, H.; Jin, S.; Xu, X. Functional Group Effects on the Photoelectronic Properties of MXene (Sc2CT2, T = O, F, OH) and Their Possible Photocatalytic Activities. *Sci. Rep.* **2017**, *7*, 15095. [CrossRef]
51. Zhao, D.; Huang, C.; Quan, X.; Li, L.; Wang, Y.; Zhou, J. Lysozyme Adsorption on Different Functionalized MXenes: A Multiscale Simulation Study. *Langmuir* **2021**, *37*, 5932–5942. [CrossRef]
52. Song, H.; Jiang, D.E. First principles insights into stability of defected MXenes in water. *Nanoscale* **2023**, *15*, 16010–16015. [CrossRef] [PubMed]
53. Sun, S.; Sha, X.; Liang, J.; Yang, G.; Hu, X.; Wen, Y.; Liu, M.; Zhou, N.; Zhang, X.; Wei, Y. Construction of ionic liquid functionalized MXene with extremely high adsorption capacity towards iodine via the combination of mussel-inspired chemistry and Michael addition reaction. *J. Colloid Interface Sci.* **2021**, *601*, 294–304. [CrossRef] [PubMed]
54. Yu, J.; Jin, Y.; Hu, M.; Ren, W.; Xie, Y.; Wang, Y. BC6N as a promising sulfur host material for lithium-sulfur batteries. *Appl. Surf. Sci.* **2022**, *577*, 151843. [CrossRef]

55. Jiang, Y.; Liu, Z.; Zhou, H.; Sharma, A.; Deng, J.; Ke, C. Physical adsorption and oxidation of ultra-thin MoS2 crystals: Insights into surface engineering for 2D electronics and beyond. *Nanotechnology* **2023**, *34*, 405701. [CrossRef]
56. Lee, T.W.; Chen, C.C.; Chen, C. Chemical Stability and Transformation of Molybdenum Disulfide Nanosheets in Environmental Media. *Environ. Sci. Technol.* **2019**, *53*, 6282–6291. [CrossRef]
57. Zhang, W.; Matsuda, K.; Miyauchi, Y. Photostability of Monolayer Transition-Metal Dichalcogenides in Ambient Air and Acidic/Basic Aqueous Solutions. *ACS Omega* **2019**, *4*, 10322–10327. [CrossRef]
58. Zhao, X.; Dall'Agnese, C.; Chu, X.; Zhao, S.; Chen, G.; Gogotsi, Y.; Gao, Y.; Dall'Agnese, Y. Electrochemical Behavior of $Ti_3C_2T_x$ MXene in Environmentally Friendly Methanesulfonic Acid Electrolyte. *ChemSusChem* **2019**, *12*, 4480–4486. [CrossRef]
59. Mehdi, S.M.Z.; Ghulam Abbas, H.; Ali, M.; Rizvi, S.B.H.; Choi, S.R.; Goak, J.C.; Seo, Y.; Kumar, S.; Lee, N. Enhanced Electrochemical Performance and Theoretical Insights of Ni-Intercalated $Ti_3C_2T_x$ MX ene. *ENERGY Environ. Mater.* **2025**. [CrossRef]
60. Huang, P.; Jia, H.; Wang, T.; Xu, Y.; Zhang, L.; Wei, X.; Jia, H.; Wen, S.; Lv, K.; Liu, D. Effects of Modification Degrees on the Colloidal Stability of Amphiphilic Janus Graphene Oxide in Aqueous Solution with and without Electrolytes. *Langmuir* **2021**, *37*, 10061–10070. [CrossRef]
61. Kim, C.; Lee, J.; Wang, W.; Fortner, J. Organic functionalized graphene oxide behavior in water. *Nanomaterials* **2020**, *10*, 1228. [CrossRef]
62. Iakunkov, A.; Nordenström, A.; Boulanger, N.; Hennig, C.; Baburin, I.; Talyzin, A.V. Temperature-dependent swelling transitions in MXene $Ti_3C_2T_x$. *Nanoscale* **2022**, *14*, 10940–10949. [CrossRef] [PubMed]
63. Wen, J.; Fu, Q.; Wu, W.; Gao, H.; Zhang, X.; Wang, B. Understanding the different diffusion mechanisms of hydrated protons and potassium ions in titanium carbide mxene. *ACS Appl. Mater. Interfaces* **2019**, *11*, 7087–7095. [CrossRef] [PubMed]
64. Liu, X.; Wu, W.; Guo, B.; Cui, M.; Ma, H.; Zhang, Z.; Zhang, R. Facile fabrication of ultrathin graphene film with ultrahigh electrical conductivity and superb electromagnetic interference shielding effectiveness. *J. Mater. Chem. C* **2021**, *9*, 214–222. [CrossRef]
65. Guo, T.; Zhou, D.; Deng, S.; Jafarpour, M.; Avaro, J.; Neels, A.; Heier, J.; Zhang, C. Rational Design of $Ti_3C_2T_x$ MXene Inks for Conductive, Transparent Films. *ACS Nano* **2023**, *17*, 3737–3749. [CrossRef]
66. Ranjan, B.; Kaur, D. Achieving enhanced pseudocapacitance in MoS2 nanowires rationally sputtered over NiMnIn shape memory alloy for flexible Na-ion supercapacitor. *J. Energy Storage* **2023**, *71*, 108122. [CrossRef]
67. Lee, J.J.; Chae, S.-H.; Lee, J.J.; Lee, M.S.; Yoon, W.; Kwac, L.K.; Kim, H.G.; Shin, H.K. Waste-Wood-Isolated Cellulose-Based Activated Carbon Paper Electrodes with Graphene Nanoplatelets for Flexible Supercapacitors. *Molecules* **2023**, *28*, 7822. [CrossRef]
68. Wu, W.; Wang, C.; Zhao, C.; Wei, D.; Zhu, J.; Xu, Y. Facile strategy of hollow polyaniline nanotubes supported on Ti3C2-MXene nanosheets for High-performance symmetric supercapacitors. *J. Colloid Interface Sci.* **2020**, *580*, 601–613. [CrossRef]
69. Park, S.; Park, B.; Jeon, S.-P.; Kang, Y.; Kim, J.; Park, S.K.; Kim, Y.-H. Effects of Ti Doping on the Electrical Properties and Gate-Bias Stability of Amorphous Zinc–Tin–Oxide Thin-Film Transistors. *ACS Appl. Electron. Mater.* **2023**, *5*, 3416–3425. [CrossRef]
70. Xu, X.; Jiang, H.; Liu, W.; Wang, S.; Wang, X.; Wang, M.; Ma, W.; Sun, G.; Liu, J. Design of $Ti_3C_2T_x/SnO_2$-Selective Ethanolamine Sensor. *ACS Appl. Nano Mater.* **2024**, *7*, 4324–4335. [CrossRef]
71. Shi, M.; Wang, R.; Li, L.; Chen, N.; Xiao, P.; Yan, C.; Yan, X. Redox-Active Polymer Integrated with MXene for Ultra-Stable and Fast Aqueous Proton Storage. *Adv. Funct. Mater.* **2023**, *33*. [CrossRef]
72. Li, J.; Song, J.; Luo, L.; Zhang, H.; Feng, J.; Zhao, X.; Guo, X.; Dong, H.; Chen, S.; Liu, H.; et al. Synergy of MXene with Se Infiltrated Porous N-Doped Carbon Nanofibers as Janus Electrodes for High-Performance Sodium/Lithium–Selenium Batteries. *Adv. Energy Mater.* **2022**, *12*, 2200894. [CrossRef]
73. Lu, C.; Li, A.; Li, G.; Yan, Y.; Zhang, M.; Yang, Q.; Zhou, W.; Guo, L. S-Decorated Porous Ti_3C_2 MXene Combined with In Situ Forming Cu_2Se as Effective Shuttling Interrupter in Na–Se Batteries. *Adv. Mater.* **2021**, *33*. [CrossRef]
74. Liu, N.; Li, Q.; Wan, H.; Chang, L.; Wang, H.; Fang, J.; Ding, T.; Wen, Q.; Zhou, L.; Xiao, X. High-temperature stability in air of $Ti_3C_2T_x$ MXene-based composite with extracted bentonite. *Nat. Commun.* **2022**, *13*, 5551. [CrossRef]
75. Wang, M.; Zhang, T.; Meng, Z.; Wang, C.; Dong, W.; Liu, J.; Yang, S.; Hou, X.; Cheng, X.; Liu, W.; et al. Self-intercepting interference of hydrogen-bond induced flexible hybrid film to facilitate lithium extraction. *Chem. Eng. J.* **2023**, *458*, 141403. [CrossRef]
76. Hakim, M.W.; Fatima, S.; Tahir, R.; Iqbal, M.Z.; Li, H.; Rizwan, S. Ni-intercalated $Mo_2TiC_2T_x$ free-standing MXene for excellent gravimetric capacitance prepared via electrostatic self-assembly. *J. Energy Storage* **2023**, *61*, 106662. [CrossRef]
77. Tran, M.H.; Schäfer, T.; Shahraei, A.; Dürrschnabel, M.; Molina-Luna, L.; Kramm, U.I.; Birkel, C.S. Adding a New Member to the MXene Family: Synthesis, Structure, and Electrocatalytic Activity for the Hydrogen Evolution Reaction of $V_4C_3T_x$. *ACS Appl. Energy Mater.* **2018**, *1*, 3908–3914. [CrossRef]
78. Bin, X.; Sheng, M.; Luo, Y.; Que, W. Self-Assembling Delaminated $V_4C_3T_x$ MXene into Highly Stable Pseudocapacitive Flexible Film Electrode for Supercapacitors. *Adv. Mater. Interfaces* **2022**, *9*, 2200231. [CrossRef]
79. Zhou, J.; Lin, S.; Huang, Y.; Tong, P.; Zhao, B.; Zhu, X.; Sun, Y. Synthesis and lithium ion storage performance of two-dimensional V_4C_3 MXene. *Chem. Eng. J.* **2019**, *373*, 203–212. [CrossRef]

80. Lin, Z.; Barbara, D.; Taberna, P.-L.; Van Aken, K.L.; Anasori, B.; Gogotsi, Y.; Simon, P. Capacitance of $Ti_3C_2T_x$ MXene in ionic liquid electrolyte. *J. Power Sources* **2016**, *326*, 575–579. [CrossRef]
81. Shao, H.; Lin, Z.; Xu, K.; Taberna, P.L.; Simon, P. Electrochemical study of pseudocapacitive behavior of $Ti_3C_2T_x$ MXene material in aqueous electrolytes. *Energy Storage Mater.* **2019**, *18*, 456–461. [CrossRef]
82. Ghotia, S.; Kumar, A.; Sudarsan, V.; Dwivedi, N.; Singh, S.; Kumar, P. Multilayered $Ti_3C_2T_x$ MXenes: A prominent materials for hydrogen storage. *Int. J. Hydrogen Energy* **2024**, *52*, 100–107. [CrossRef]
83. Anasori, B.; Xie, Y.; Beidaghi, M.; Lu, J.; Hosler, B.C.; Hultman, L.; Kent, P.R.C.; Gogotsi, Y.; Barsoum, M.W. Two-Dimensional, Ordered, Double Transition Metals Carbides (MXenes). *ACS Nano* **2015**, *9*, 9507–9516. [CrossRef]
84. Chen, C.; Xie, X.; Anasori, B.; Sarycheva, A.; Makaryan, T.; Zhao, M.; Urbankowski, P.; Miao, L.; Jiang, J.; Gogotsi, Y. MoS_2-on-MXene Heterostructures as Highly Reversible Anode Materials for Lithium-Ion Batteries. *Angew. Chemie-Int. Ed.* **2018**, *57*, 1846–1850. [CrossRef]
85. Deysher, G.; Shuck, C.E.; Hantanasirisakul, K.; Frey, N.C.; Foucher, A.C.; Maleski, K.; Sarycheva, A.; Shenoy, V.B.; Stach, E.A.; Anasori, B.; et al. Synthesis of Mo4VAlC4 MAX Phase and Two-Dimensional Mo_4VC_4 MXene with Five Atomic Layers of Transition Metals. *ACS Nano* **2020**, *14*, 204–217. [CrossRef]
86. Hussain, I.; Rehman, F.; Saraf, M.; Zhang, T.; Wang, R.; Das, T.; Luo, Z.; Gogotsi, Y.; Zhang, K. Electrochemical Properties of $Mo_4VC_4T_x$ MXene in Aqueous Electrolytes. *ACS Appl. Mater. Interfaces* **2024**, *16*, 38053–38060. [CrossRef]
87. Hu, Q.; Sun, D.; Wu, Q.; Wang, H.; Wang, L.; Liu, B.; Zhou, A.; He, J. MXene: A new family of promising hydrogen storage medium. *J. Phys. Chem. A* **2013**, *117*, 14253–14260. [CrossRef] [PubMed]
88. Fang, Y.; Hu, R.; Liu, B.; Zhang, Y.; Zhu, K.; Yan, J.; Ye, K.; Cheng, K.; Wang, G.; Cao, D. MXene-derived TiO_2/reduced graphene oxide composite with an enhanced capacitive capacity for Li-ion and K-ion batteries. *J. Mater. Chem. A* **2019**, *7*, 5363–5372. [CrossRef]
89. Wang, G.; Yang, Z.; Nie, X.; Wang, M.; Liu, X. A Flexible Supercapacitor Based on Niobium Carbide MXene and Sodium Anthraquinone-2-Sulfonate Composite Electrode. *Micromachines* **2023**, *14*, 1515. [CrossRef] [PubMed]
90. Jiang, Y.; Tian, M.; Wang, H.; Wei, C.; Sun, Z.; Rummeli, M.H.; Strasser, P.; Sun, J.; Yang, R. Mildly Oxidized MXene (Ti_3C_2, Nb_2C, and V_2C) Electrocatalyst via a Generic Strategy Enables Longevous Li-O_2 Battery under a High Rate. *ACS Nano* **2021**, *15*, 19640–19650. [CrossRef] [PubMed]
91. Yazdanparast, S.; Soltanmohammad, S.; Fash-White, A.; Tucker, G.J.; Brennecka, G.L. Synthesis and Surface Chemistry of 2D TiVC Solid-Solution MXenes. *ACS Appl. Mater. Interfaces* **2020**, *12*, 20129–20137. [CrossRef]
92. Baig, M.M.; Gul, I.H.; Baig, S.M.; Shahzad, F. 2D MXenes: Synthesis, properties, and electrochemical energy storage for supercapacitors—A review. *J. Electroanal. Chem.* **2022**, *904*, 115920. [CrossRef]
93. Shankar, S.; Murphy, B.B.; Driscoll, N.; Shekhirev, M.; Valurouthu, G.; Shevchuk, K.; Anayee, M.; Cimino, F.; Gogotsi, Y.; Vitale, F. Effect of the deposition process on the stability of $Ti_3C_2T_x$ MXene films for bioelectronics. *2D Mater.* **2023**, *10*, 44001. [CrossRef] [PubMed]
94. Shen, S.; Ke, T.; Rajavel, K.; Yang, K.; Lin, D. Dispersibility and Photochemical Stability of Delaminated MXene Flakes in Water. *Small* **2020**, *16*, 2002433. [CrossRef] [PubMed]
95. Choi, J.; Oh, M.S.; Cho, A.; Ryu, J.; Kim, Y.J.; Kang, H.; Cho, S.Y.; Im, S.G.; Kim, S.J.; Jung, H.T. Simple Approach to Enhance Long-Term Environmental Stability of MXene Using Initiated Chemical Vapor Deposition Surface Coating. *ACS Nano* **2023**, *17*, 10898–10905. [CrossRef]
96. Sun, X.; Li, Y.; Wang, Y.; Liu, Z.; Dong, K.; Zhang, S. Effect of Interlayer Spaces and Interfacial Structures on High-Performance MXene/Ionic Liquid Supercapacitors: A Molecular Dynamics Simulation. *Langmuir* **2024**, *40*, 2220–2229. [CrossRef]
97. Benchakar, M.; Loupias, L.; Garnero, C.; Bilyk, T.; Morais, C.; Canaff, C.; Guignard, N.; Morisset, S.; Pazniak, H.; Hurand, S.; et al. One MAX phase, different MXenes: A guideline to understand the crucial role of etching conditions on $Ti_3C_2T_x$ surface chemistry. *Appl. Surf. Sci.* **2020**, *530*, 147209. [CrossRef]
98. Gurzęda, B.; Boulanger, N.; Nordenström, A.; Dejoie, C.; Talyzin, A.V. Pristine MXene: In Situ XRD Study of MAX Phase Etching with HCl+LiF Solution. *Adv. Sci.* **2024**, *11*, 2408448. [CrossRef]
99. Carey, M.S.; Barsoum, M.W. Scalable and sustainable production of $Ti_3C_2T_z$ MXene and fluorine recovery from wastewater through cryolite precipitation. *RSC Adv.* **2022**, *12*, 30846–30850. [CrossRef]
100. Ma, Q.; Gao, J.; Moussa, B.; Young, J.; Zhao, M.; Zhang, W. Electrosorption, Desorption, and Oxidation of Perfluoroalkyl Carboxylic Acids (PFCAs) via MXene-Based Electrocatalytic Membranes. *ACS Appl. Mater. Interfaces* **2023**, *15*, 29149–29159. [CrossRef]
101. Liu, R.; Li, J.; Li, M.; Zhang, Q.; Shi, G.; Li, Y.; Hou, C.; Wang, H. MXene-Coated Air-Permeable Pressure-Sensing Fabric for Smart Wear. *ACS Appl. Mater. Interfaces* **2020**, *12*, 46446–46454. [CrossRef]
102. Wang, T.; Wang, C.; Xu, X.; Li, Z.; Li, D. One-step electrodeposition synthesized aunps/mxene/ERGO for selectivity nitrite sensing. *Nanomaterials* **2021**, *11*, 1892. [CrossRef]

103. Jiang, X.; Jia, H.; Chen, X.; Li, J.; Chen, Y.; Jia, J.; Zhao, G.; Yu, L.; Zhu, G.; Zhu, Y. Broadening the Voltage Window of 3D-Printed MXene Micro-Supercapacitors with a Hybridized Electrolyte. *Molecules* **2024**, *29*, 1393. [CrossRef]
104. Liao, Y.; Bin, X.; Xu, J.; He, X.; Que, W. Nitrogen-Doped MXene Electrodes for High-Voltage Window Supercapacitors in Organic Electrolytes. *Chemistry* **2025**, *7*, 13. [CrossRef]
105. Jiang, X.; Wu, X.; Xie, Y.; Wang, Z.; Huang, J.; Qu, Y.; Mu, D.; Zhang, X.; Yang, W.; Zhang, H. Additive Engineering Enables Ionic-Liquid Electrolyte-Based Supercapacitors To Deliver Simultaneously High Energy and Power Density. *ACS Sustain. Chem. Eng.* **2023**, *11*, 5685–5695. [CrossRef]
106. Wang, X.; Mathis, T.S.; Li, K.; Lin, Z.; Vlcek, L.; Torita, T.; Osti, N.C.; Hatter, C.; Urbankowski, P.; Sarycheva, A.; et al. Influences from solvents on charge storage in titanium carbide MXenes. *Nat. Energy* **2019**, *4*, 241–248. [CrossRef]
107. Liu, Y.; Meng, X.; Wang, Z.; Qiu, J. Development of quasi-solid-state anode-free high-energy lithium sulfide-based batteries. *Nat. Commun.* **2022**, *13*, 4415. [CrossRef] [PubMed]
108. Karmur, R.S.; Gogoi, D.; Biswas, A.; Prathibha, C.; Das, M.R.; Ghosh, N.N. Nanocomposite having hierarchical architecture of MXene-WO_3 nanorod@rGOsponge and porous carbon for cathode and anode materials for high-performance flexible all-solid-state asymmetric supercapacitor device. *Appl. Surf. Sci.* **2023**, *623*, 157042. [CrossRef]
109. Likitaporn, C.; Okhawilai, M.; Kasemsiri, P.; Qin, J.; Potiyaraj, P.; Uyama, H. High electrolyte uptake of MXene integrated membrane separators for Zn-ion batteries. *Sci. Rep.* **2022**, *12*, 19915. [CrossRef]
110. Ionescu, D.; Kovaci, M. Prediction of the Specific Energy of Supercapacitors with Polymeric Materials Using Advanced Molecular Dynamics Simulations. *Polymers* **2024**, *16*, 3404. [CrossRef]
111. Liu, S.; Yin, T.; Li, Z.; Wang, J. Potentiometric/time resolved chronopotentiometric sensing for an all-solid-state ion-selective electrode based on MXene/MWCNTs as solid contact. *Sensors Actuators B Chem.* **2024**, *405*, 135269. [CrossRef]
112. Jia, Z.; Li, Z.; Ma, S.; Zhang, W.; Chen, Y.; Luo, Y.; Jia, D.; Zhong, B.; Razal, J.M.; Wang, X.; et al. Constructing conductive titanium carbide nanosheet (MXene) network on polyurethane/polyacrylonitrile fibre framework for flexible strain sensor. *J. Colloid Interface Sci.* **2021**, *584*, 1–10. [CrossRef] [PubMed]
113. Zhang, T.; Wang, S.; Qiu, R.; Yang, X.; Zhu, F. MXene/sPS nanocomposites: Rheological, electrical conductivity, polymorphism, mechanical, thermal, and flammability properties. *RSC Adv.* **2024**, *14*, 25793–25801. [CrossRef] [PubMed]
114. Kumar, S.; Kang, D.; Nguyen, V.H.; Nasir, N.; Hong, H.; Kim, M.; Nguyen, D.C.; Lee, Y.J.; Lee, N.; Seo, Y. Application of Titanium-Carbide MXene-Based Transparent Conducting Electrodes in Flexible Smart Windows. *ACS Appl. Mater. Interfaces* **2021**, *13*, 40976–40985. [CrossRef] [PubMed]
115. Lin, H.T.; Chuang, E.; Lin, S.C. Advancing Lithium Battery Performance through Porous Conductive Polyaniline-Modified Graphene Composites Additive. *Nanomaterials* **2024**, *14*, 509. [CrossRef]
116. Khan, S.; Alkhedhe, M.; Raza, R.; Ahmad, M.A.; Majid, A.; Tag El Din, E.M. Electrochemical Investigation of PANI:PPy/AC and PANI:PEDOT/AC Composites as Electrode Materials in Supercapacitors. *Polymers* **2022**, *14*, 1976. [CrossRef]
117. Cirillo, C.; Iuliano, M.; Scarpa, D.; Iovane, P.; Borriello, C.; Portofino, S.; Galvagno, S.; Sarno, M. Silver-Doped Reduced Graphene Oxide/PANI-DBSA-PLA Composite 3D-Printed Supercapacitors. *Nanomaterials* **2024**, *14*, 1681. [CrossRef]
118. He, T.; Li, X.; Sun, B.; Lin, L.; Guo, F.; Diao, G.; Piao, Y.; Zhang, W. Preparation of cyclodextrin polymer-functionalized polyaniline/MXene composites for high-performance supercapacitor. *RSC Adv.* **2024**, *14*, 13685–13693. [CrossRef]
119. Liu, Y.; Yuan, J.; Wang, Y.; Zheng, R.; Liu, Q.; Shang, X.; Shao, J.; Wan, Z.; Luo, J.; Jia, C. Approach to Significantly Enhancing the Electrochromic Performance of PANi by In Situ Electrodeposition of the PANi@MXene Composite Film. *ACS Appl. Mater. Interfaces* **2023**, *15*, 58940–58954. [CrossRef]
120. Guan, X.; Feng, W.; Wang, X.; Venkatesh, R.; Ouyang, J. Significant Enhancement in the Seebeck Coefficient and Power Factor of p-Type Poly(3,4-ethylenedioxythiophene):Poly(styrenesulfonate) through the Incorporation of n-Type MXene. *ACS Appl. Mater. Interfaces* **2020**, *12*, 13013–13020. [CrossRef]
121. Habibpour, S.; Zarshenas, K.; Zhang, M.; Hamidinejad, M.; Ma, L.; Park, C.B.; Yu, A. Greatly Enhanced Electromagnetic Interference Shielding Effectiveness and Mechanical Properties of Polyaniline-Grafted $Ti_3C_2T_x$ MXene-PVDF Composites. *ACS Appl. Mater. Interfaces* **2022**, *14*, 21521–21534. [CrossRef]
122. Alex, M.; Khan, K.R.B.; Al-Othman, A.; Al-Sayah, M.H.; Al Nashash, H. MXene-Based Flexible Electrodes for Electrophysiological Monitoring. *Sensors* **2024**, *24*, 3260. [CrossRef]
123. Kim, J.; Ryu, J.H.; Jang, M.; Park, S.; Kim, M.; Lee, K.H.; Choi, S.; Yoon, Y.; Jung, H.K.; Lee, S.S.; et al. One-Dimensional π-d Conjugated Coordination Polymer Intercalated MXene Compound for High-Performance Supercapacitor Electrode. *Small Methods* **2023**, *7*, 2201539. [CrossRef]
124. Liu, Y.; Dai, Z.; Zhang, W.; Jiang, Y.; Peng, J.; Wu, D.; Chen, B.; Wei, W.; Chen, X.; Liu, Z.; et al. Sulfonic-Group-Grafted $Ti_3C_2T_x$ MXene: A Silver Bullet to Settle the Instability of Polyaniline toward High-Performance Zn-Ion Batteries. *ACS Nano* **2021**, *15*, 9065–9075. [CrossRef]

125. Fu, Z.; Chen, Q.; He, J.; Li, S.; Ming, R.; Wei, Y.; Xu, Y.; Liu, J.; Zhang, L. A synergistic effect of MXene/MWCNT enables self-healable and low percolation elastomer sensor: A combined experiment and all-atom molecular dynamics simulation. *Compos. Sci. Technol.* **2023**, *242*, 110155. [CrossRef]
126. Guo, T.; Fu, M.; Zhou, D.; Pang, L.; Su, J.; Lin, H.; Yao, X.; Sombra, A.S.B. Flexible $Ti_3C_2T_x$/Graphene Films with Large-Sized Flakes for Supercapacitors. *Small Struct.* **2021**, *2*, 2100015. [CrossRef]
127. Gao, M.; Xie, Y.; Yang, W.; Lu, L. Fabrication of novel electrochemical sensor based on MXene/MWCNTs composite for sensitive detection of synephrine. *Int. J. Electrochem. Sci.* **2020**, *15*, 4619–4630. [CrossRef]
128. Shi, X.; Guo, F.; Hou, K.; Guan, G.; Lu, L.; Zhang, Y.; Xu, J.; Shang, Y. Highly Flexible All-Solid-State Supercapacitors Based on MXene/CNT Composites. *Energy Fuels* **2023**, *37*, 9704–9712. [CrossRef]
129. Chen, J.; Feng, M.; Lian, X.; Zheng, F.; Xu, C.; Wang, K.; Niu, H. Rational design of MXene/MWCNT/TOCNF film for flexible supercapacitor. *Ceram. Int.* **2024**, *50*, 29895–29903. [CrossRef]
130. Xu, S.; Wei, G.; Li, J.; Han, W.; Gogotsi, Y. Flexible MXene-graphene electrodes with high volumetric capacitance for integrated co-cathode energy conversion/storage devices. *J. Mater. Chem. A* **2017**, *5*, 17442–17451. [CrossRef]
131. Kalambate, P.K.; Dhanjai; Sinha, A.; Li, Y.; Shen, Y.; Huang, Y. An electrochemical sensor for ifosfamide, acetaminophen, domperidone, and sumatriptan based on self-assembled MXene/MWCNT/chitosan nanocomposite thin film. *Microchim. Acta* **2020**, *187*, 402. [CrossRef]
132. Li, Y.; Yang, R.; Xie, J.; Li, J.; Huang, H.; Liang, X.; Huang, D.; Lan, Z.; Liu, H.; Li, G.; et al. Potassium Ion-Assisted Self-Assembled MXene-K-CNT Composite as High-Quality Sulfur-Loaded Hosts for Lithium-Sulfur Batteries. *ACS Appl. Mater. Interfaces* **2024**, *16*, 39771–39783. [CrossRef]
133. Chen, K.; Yan, X.; Li, J.; Jiao, T.; Cai, C.; Zou, G.; Wang, R.; Wang, M.; Zhang, L.; Peng, Q. Preparation of self-assembled composite films constructed by chemically-modified mxene and dyes with surface-enhanced raman scattering characterization. *Nanomaterials* **2019**, *9*, 284. [CrossRef]
134. Pan, Z.; Ji, X. Facile synthesis of nitrogen and oxygen co-doped C@Ti_3C_2 MXene for high performance symmetric supercapacitors. *J. Power Sources* **2019**, *439*, 227068. [CrossRef]
135. Afolabi, M.A.; Xiao, D.; Chen, Y. The Impact of Surface Chemistry and Synthesis Conditions on the Adsorption of Antibiotics onto MXene Membranes. *Molecules* **2024**, *29*, 148. [CrossRef]
136. Khaledialidusti, R.; Mahdavi, E.; Barnoush, A. Stabilization of 2D graphene, functionalized graphene, and Ti_2CO_2 (MXene) in super-critical CO_2: A molecular dynamics study. *Phys. Chem. Chem. Phys.* **2019**, *21*, 12968–12976. [CrossRef]
137. Ali, A.; Hantanasirisakul, K.; Abdala, A.; Urbankowski, P.; Zhao, M.Q.; Anasori, B.; Gogotsi, Y.; Aïssa, B.; Mahmoud, K.A. Effect of Synthesis on Performance of MXene/Iron Oxide Anode Material for Lithium-Ion Batteries. *Langmuir* **2018**, *34*, 11325–11334. [CrossRef] [PubMed]
138. Wojciechowski, T.; Rozmysłowska-Wojciechowska, A.; Matyszczak, G.; Wrzecionek, M.; Olszyna, A.; Peter, A.; Mihaly-Cozmuta, A.; Nicula, C.; Mihaly-Cozmuta, L.; Podsiadło, S.; et al. Ti_2C MXene Modified with Ceramic Oxide and Noble Metal Nanoparticles: Synthesis, Morphostructural Properties, and High Photocatalytic Activity. *Inorg. Chem.* **2019**, *58*, 7602–7614. [CrossRef] [PubMed]
139. Rozmysłowska-Wojciechowska, A.; Karwowska, E.; Poźniak, S.; Wojciechowski, T.; Chlubny, L.; Olszyna, A.; Ziemkowska, W.; Jastrzębska, A.M. Influence of modification of Ti_3C_2 MXene with ceramic oxide and noble metal nanoparticles on its antimicrobial properties and ecotoxicity towards selected algae and higher plants. *RSC Adv.* **2019**, *9*, 4092–4105. [CrossRef]
140. Zhang, X.; Li, J.; Han, L.; Li, H.; Wang, J.; Lu, T.; Pan, L. In-situ fabrication of few-layered MoS_2 wrapped on TiO_2-decorated MXene as anode material for durable lithium-ion storage. *J. Colloid Interface Sci.* **2021**, *604*, 30–38. [CrossRef]
141. Yuan, W.; Cheng, L.; Zhang, B.; Wu, H. 2D-Ti_3C_2 as hard, conductive substrates to enhance the electrochemical performance of MnO_2 for supercapacitor applications. *Ceram. Int.* **2018**, *44*, 17539–17543. [CrossRef]
142. Tang, H.; Jiang, M.; Ren, E.; Zhang, Y.; Lai, X.; Cui, C.; Jiang, S.; Zhou, M.; Qin, Q.; Guo, R. Integrate electrical conductivity and Li+ ion mobility into hierarchical heterostructure Ti_3C_2@CoO/ZnO composites toward high-performance lithium ion storage. *Energy* **2020**, *212*, 118696. [CrossRef]
143. Seredych, M.; Shuck, C.E.; Pinto, D.; Alhabeb, M.; Precetti, E.; Deysher, G.; Anasori, B.; Kurra, N.; Gogotsi, Y. High-Temperature Behavior and Surface Chemistry of Carbide MXenes Studied by Thermal Analysis. *Chem. Mater.* **2019**, *31*, 3324–3332. [CrossRef]
144. Guo, J.; Legum, B.; Anasori, B.; Wang, K.; Lelyukh, P.; Gogotsi, Y.; Randall, C.A. Cold Sintered Ceramic Nanocomposites of 2D MXene and Zinc Oxide. *Adv. Mater.* **2018**, *30*, 1801846. [CrossRef] [PubMed]
145. Song, D.; Jiang, X.; Li, Y.; Lu, X.; Luan, S.; Wang, Y.; Li, Y.; Gao, F. Metal−organic frameworks-derived MnO_2/Mn_3O_4 microcuboids with hierarchically ordered nanosheets and Ti_3C_2 MXene/Au NPs composites for electrochemical pesticide detection. *J. Hazard. Mater.* **2019**, *373*, 367–376. [CrossRef] [PubMed]
146. Myndrul, V.; Coy, E.; Babayevska, N.; Zahorodna, V.; Balitskyi, V.; Baginskiy, I.; Gogotsi, O.; Bechelany, M.; Giardi, M.T.; Iatsunskyi, I. MXene nanoflakes decorating ZnO tetrapods for enhanced performance of skin-attachable stretchable enzymatic electrochemical glucose sensor. *Biosens. Bioelectron.* **2022**, *207*, 114141. [CrossRef] [PubMed]

147. Zhang, X.; Javed, M.S.; Ren, H.; Batool, S.; Ahmad, A.; Tao, R.; Albaqami, M.D.; Khan, S.; Wang, X.; Han, W. Optimization of $Ti_3C_2T_x$ performance through synergistic enhancement of GeOx/Ti3C2Tx heterostructures for ammonium-ion storage. *Chem. Eng. J.* **2025**, *504*, 158582. [CrossRef]
148. Rajeeve, A.D.; Yamuna, R.; Vinoba, M.; Bhagiyalakshmi, M. β-Cyclodextrin-Stabilized CuO/MXene Nanocomposite as an Electrode Material for High-Performance Supercapacitors. *Langmuir* **2023**, *39*, 17688–17699. [CrossRef]
149. Shao, H.; Xu, K.; Wu, Y.C.; Iadecola, A.; Liu, L.; Ma, H.; Qu, L.; Raymundo-Piñero, E.; Zhu, J.; Lin, Z.; et al. Unraveling the charge storage mechanism of Ti_3C_2T xmxene electrode in acidic electrolyte. *ACS Energy Lett.* **2020**, *5*, 2873–2880. [CrossRef]
150. Sharma, A.; Mane, P.; Chakraborty, B.; Rout, C.S. 1T-VS_2/MXene Hybrid as a Superior Electrode Material for Asymmetric Supercapacitors: Experimental and Theoretical Investigations. *ACS Appl. Energy Mater.* **2021**, *4*, 14198–14209. [CrossRef]
151. Siddu, P.; Sree Raj, K.A.; Radhakrishnan, S.; Mun Jeong, S.; Sekhar Rout, C. 3D Ternary Hybrid of VSe_2/e-MXene/CNT with a Promising Energy Storage Performance for High Performance Asymmetric Supercapacitor. *Batter. Supercaps* **2024**, *8*, e202400466. [CrossRef]
152. Wang, Y.; Wang, B.; Yang, G.; Zhang, L.; Zhang, K.; Lucia, L.A.; Meng, L.; Wang, X.; Chen, J. Multifunctional hydrogel enabled by tannin derived nanoparticles system for the application of strain sensing and human machine interfaces. *Colloids Surfaces A Physicochem. Eng. Asp.* **2025**, *711*, 136367. [CrossRef]
153. Chen, Y.; Hao, Y.; Feng, L.; Meng, J.; Yang, Z.; Wu, H.; Li, P.; Zhu, Z.; Zhao, B.; Wei, Q. A flexible multifunctional triboelectric nanogenerator based on bio-inspired nanocellulose/tannic acid@MXene-composited hydrogel for human healthcare. *Int. J. Biol. Macromol.* **2025**, *306*, 141261. [CrossRef]
154. Zeng, H.; Zhang, L.; Wu, T.; Song, H.; Wan, Y.; Zhang, M. High-Performance Conductive Hydrogel Prepared by an Electrohydrodynamic Printing Method for Strain Sensors and Self-Powered Triboelectric Nanogenerator. *ACS Appl. Nano Mater.* **2025**, *8*, 589–601. [CrossRef]
155. Salami, N. First-principles realistic prediction of gas adsorption on two-dimensional Vanadium Carbide (MXene). *Appl. Surf. Sci.* **2022**, *581*, 152105. [CrossRef]
156. Mondal, A.; Faraz, M.; Dahiya, M.; Khare, N. Double-Layer Electronegative Structure-Based Triboelectric Nanogenerator for Enhanced Performance Using Combined Effect of Enhanced Charge Generation and Improved Charge Trapping. *ACS Appl. Mater. Interfaces* **2024**, *16*, 50659–50670. [CrossRef] [PubMed]
157. Simon, P.; Gogotsi, Y. Materials for electrochemical capacitors. *Nat. Mater.* **2008**, *7*, 845–854. [CrossRef]
158. Xu, H.; Fan, J.; Pang, D.; Zheng, Y.; Chen, G.; Du, F.; Gogotsi, Y.; Dall'Agnese, Y.; Gao, Y. Synergy of ferric vanadate and MXene for high performance Li- and Na-ion batteries. *Chem. Eng. J.* **2022**, *436*, 135012. [CrossRef]
159. Zhang, H.; Li, Z.; Hou, Z.; Mei, H.; Feng, Y.; Xu, B.; Sun, D. Self-assembly of MOF on MXene nanosheets and in-situ conversion into superior nickel phosphates/MXene battery-type electrode. *Chem. Eng. J.* **2021**, *425*, 130602. [CrossRef]
160. Akıllı, A.; Taymaz, B.H.; Eskizeybek, V.; Kamış, H. Enhanced performance of MXene-based supercapacitor via new activated carbon-nafion composite cathode. *J. Phys. Chem. Solids* **2025**, *199*, 112523. [CrossRef]
161. Shivade, D.S.; Kurade, A.N.; Bhosale, R.K.; Kundale, S.S.; Shelake, A.R.; Patil, A.D.; Waifalkar, P.P.; Kamat, R.K.; Teli, A.M.; Dongale, T.D. Folic acid-assisted in situ solvothermal synthesis of Ni-MOF/MXene composite for high-performance supercapacitors. *J. Energy Storage* **2024**, *100*, 113754. [CrossRef]
162. Baasanjav, E.; Raj, K.A.S.; Hakkeem, H.; Rout, C.S.; Jeong, S.M. High-performance asymmetric supercapacitors based on 2D MXene/NiCoP hybrid and ZIF derived porous nanocarbon. *J. Mater. Sci. Technol.* **2025**, *228*, 42–53. [CrossRef]
163. Wang, Y.; Chen, N.; Zhou, B.; Zhou, X.; Pu, B.; Bai, J.; Tang, Q.; Liu, Y.; Yang, W. NH_3-Induced In Situ Etching Strategy Derived 3D-Interconnected Porous MXene/Carbon Dots Films for High Performance Flexible Supercapacitors. *Nano-Micro Lett.* **2023**, *15*, 231. [CrossRef] [PubMed]
164. Li, Z.; Li, J.; Wu, B.; Wei, H.; Guo, H.; El-Bahy, Z.M.; Liu, B.; He, M.; Melhi, S.; Shi, X.; et al. Interfacial-engineered robust and high performance flexible polylactic acid/polyaniline/MXene electrodes for high-perfarmance supercapacitors. *J. Mater. Sci. Technol.* **2024**, *203*, 201–210. [CrossRef]
165. Zhang, S.; Li, X.; Gao, Y.; Li, L.; Bao, L.; Li, X. Physicochemical double protection enables stable MXene for high-rate performance hybrid supercapacitors. *J. Mater. Sci. Technol.* **2025**, *211*, 89–97. [CrossRef]
166. Li, J.; Qiang, X.; Jia, B.; Wang, L.; Wu, X. Etching and surface self-assembly of Ni-MOF/MXene hybrids for excellent flexible Pseudocapacitance. *Appl. Surf. Sci.* **2025**, *695*, 162867. [CrossRef]
167. Xu, C.; Tong, L.; Zhang, W.; Zhao, X.; Yang, L.; Yin, S. One-step synthesis of g-C3N4/TiVCTx MXene electrodes for lithium-ion batteries and supercapacitors. *Chem. Eng. J.* **2024**, *497*, 154449. [CrossRef]
168. Yu, L.; He, X.; Tang, L.; Wang, X.; Cai, W.; He, Y.; Sun, Y.; Zhu, G.; Rosen, J.; Jin, H. Understanding mechanisms of fast sodium storage kinetics for MXene/MoS_2@C in ether electrolytes. *J. Power Sources* **2025**, *641*, 236852. [CrossRef]
169. Yuan, Z.; Liu, Y.; Yue, M.; Cao, Y.; Wang, G.; Wang, Y. Encapsulating $FeSe_2$ nanorods in Na+ pre-intercalated 3D porous Ti3C2Tx MXene nanostructures for advanced sodium storage performance. *J. Power Sources* **2025**, *640*, 236679. [CrossRef]

170. Pathak, D.D.; Neem, M.; Kumar, G.; Modak, B.; Neogi, S.; Mandal, B.P. Diamondoid covalent organic framework-MXene composite for cathode host in lithium sulfur battery. *J. Energy Storage* **2025**, *117*, 116176. [CrossRef]
171. Chen, L.; Chen, X.; Xiao, J. Flower-like $Ti_3C_2T_x$-TiO_2 modified with ZnS nanoparticles as adsorption-catalytic cathodic material for lithium–sulfur batteries. *J. Energy Storage* **2025**, *118*, 116241. [CrossRef]
172. Wei, J.; Cao, H.; Tian, Y.; Zhang, X. MXene-encapsulated titanium-niobium oxide microspheres for fast and stable lithium storage. *Electrochim. Acta* **2023**, *464*, 142957. [CrossRef]
173. Luo, A.; CUI, Y.; Wang, J.; Ju, Z.; Zhuang, Q.; Shi, Y. SnS_2 anchored on MXene etched by hydrofluoric acid for sodium-ion battery anode material. *Solid State Ionics* **2023**, *399*, 116271. [CrossRef]
174. Niu, Y.; Feng, W.; Lei, Z.; Hu, W.; Zheng, X.; Su, W.; Zhang, L. MXene surface-attached Ni_2P on lithium-sulfur battery catalytic effect. *J. Electroanal. Chem.* **2023**, *946*, 117743. [CrossRef]
175. Wang, M.; Wang, X.; Nan, Y.; Zhou, H.; Xu, H. Enhanced of ZIF-8 and MXene decorated triboelectric nanogenerator for droplet energy harvesting. *Chem. Eng. J.* **2025**, *506*, 160137. [CrossRef]
176. Wei, R.; Sun, S. A MXene-based double-network conductive hydrogel triboelectric nanogenerator for intelligent sports monitoring. *Energy Reports* **2025**, *13*, 3773–3781. [CrossRef]
177. Zhang, D.; Yu, L.; Wang, D.; Yang, Y.; Mi, Q.; Zhang, J. Multifunctional latex/ polytetrafluoroethylene-based triboelectric nanogenerator for self-powered organ-like mxene/metal-organic framework-derived cuo nanohybrid ammonia sensor. *ACS Nano* **2021**, *15*, 2911–2919. [CrossRef]
178. Wang, L.; Gao, Y.; Luo, J.; Xu, W.; Zhang, C.; Yuan, H.; Zhang, Y.; Pang, Y. High-performance triboelectric nanogenerator based on NH2-MXene/TiO_2@sodium alginate composite film for self-powered cathodic protection. *Chem. Eng. J.* **2025**, *506*, 159837. [CrossRef]
179. Anwer, S.; Umair Khan, M.; Alazzam, A.; Mohammad, B.; Abu Nada, E. 2D $Ti_3C_2T_x$-MXene and its superstructures as dual-function electrodes for triboelectric nanogenerators for self-powered electronics. *Chem. Eng. J.* **2024**, *502*, 157985. [CrossRef]
180. Jalali, A.; Gupta, T.; Pakharenko, V.; Rejeb, Z.B.; Kheradmandkeysomi, M.; Sain, M.; Park, C.B. Lightweight 3D-printed chitosan/MXene aerogels for advanced electromagnetic shielding, energy harvesting, and thermal management. *Carbohydr. Polym.* **2025**, *352*, 123252. [CrossRef]
181. Sarikurt, S.; Çakir, D.; Keçeli, M.; Sevik, C. The influence of surface functionalization on thermal transport and thermoelectric properties of MXene monolayers. *Nanoscale* **2018**, *10*, 8859–8868. [CrossRef] [PubMed]
182. Liu, L.; Zschiesche, H.; Antonietti, M.; Daffos, B.; Tarakina, N.V.; Gibilaro, M.; Chamelot, P.; Massot, L.; Duployer, B.; Taberna, P.L.; et al. Tuning the Surface Chemistry of MXene to Improve Energy Storage: Example of Nitrification by Salt Melt. *Adv. Energy Mater.* **2023**, *13*, 2202709. [CrossRef]
183. Yu, K.; Ren, J.; Liao, W.; Hu, B.; Bai, C.; Li, Z.; Zhang, X.; Chhattal, M.; Li, N.; Qiang, L. Maintaining the 2D Structure of MXene via Self-Assembled Monolayers for Efficient Lubrication in High Humidity. *Small* **2024**, *20*, 2402143. [CrossRef]
184. Wang, L.; Gao, S.; Li, W.; Zhu, A.; Li, H.; Zhao, C.; Zhang, H.; Wang, W.-H.; Wang, W. Machine learning assisted screening of MXenes pseudocapacitive materials. *J. Power Sources* **2023**, *564*, 232834. [CrossRef]
185. Li, X.; Qiu, J.; Cui, H.; Chen, X.; Yu, J.; Zheng, K. Machine Learning Accelerated Discovery of Functional MXenes with Giant Piezoelectric Coefficients. *ACS Appl. Mater. Interfaces* **2024**, *16*, 12731–12743. [CrossRef]
186. Shrestha, S.; Barvenik, K.J.; Chen, T.; Yang, H.; Li, Y.; Kesavan, M.M.; Little, J.M.; Whitley, H.C.; Teng, Z.; Luo, Y.; et al. Machine intelligence accelerated design of conductive MXene aerogels with programmable properties. *Nat. Commun.* **2024**, *15*, 4685. [CrossRef]

Disclaimer/Publisher's Note: The statements, opinions and data contained in all publications are solely those of the individual author(s) and contributor(s) and not of MDPI and/or the editor(s). MDPI and/or the editor(s) disclaim responsibility for any injury to people or property resulting from any ideas, methods, instructions or products referred to in the content.